



## Research paper

# Numerical modeling of 3-D inclusions and voids by a novel adaptive XFEM



Zhen Wang<sup>a</sup>, Tiantang Yu<sup>a,\*\*</sup>, Tinh Quoc Bui<sup>b,c,\*</sup>, Ngoc Anh Trinh<sup>d</sup>,  
Nguyen Thi Hien Luong<sup>e</sup>, Nguyen Dinh Duc<sup>f,g</sup>, Duc Hong Doan<sup>f</sup>

<sup>a</sup> Department of Engineering Mechanics, Hohai University, Nanjing 210098, PR China

<sup>b</sup> Institute for Research and Development, Duy Tan University, Da Nang City, Vietnam

<sup>c</sup> Department of Civil and Environmental Engineering, Tokyo Institute of Technology, 2-12-1-W8-22, Ookayama, Meguro-ku, Tokyo 152-8552, Japan

<sup>d</sup> Department of Mechanics, Faculty of Mathematics and Computer Science, University of Science – VNUHCM, Vietnam

<sup>e</sup> Department of Civil Engineering, Ho Chi Minh City University of Technology- VNUHCM, Vietnam

<sup>f</sup> Advanced Materials and Structures Laboratory, University of Engineering and Technology, Vietnam National University, Vietnam

<sup>g</sup> Infrastructure Engineering Program-VNU-Hanoi, Vietnam-Japan University (VJU), My Dinh 1, Tu Liem, Hanoi, Vietnam

## ARTICLE INFO

## Article history:

Received 8 April 2016

Revised 2 September 2016

Accepted 25 September 2016

## Keywords:

XFEM

Three-dimension

Error estimation

Adaptive

Variable-node hexahedron element

Inclusions

Holes

## ABSTRACT

This paper describes an adaptive numerical framework for modeling arbitrary inclusions and holes in three-dimensional (3-D) solids based on a rigorous combination of local enriched partition-of-unity method, a *posteriori* error estimation scheme, and the variable-node hexahedron elements. In this new setting, a *posteriori* error estimation scheme driven by a recovery strain procedure in terms of extended finite element method (XFEM) is taken for adaptive purpose (local mesh refinement). Refinement is only performed where it is needed, e.g., the vicinity of the internal boundaries, through an error indicator. To treat the mismatch of different meshes-scale in 3-D, the variable-node hexahedron elements based on the generic point interpolation are thus integrated into the present formulation. The merits of the proposed approach such as its accuracy, effectiveness and performance are demonstrated through a series of representative numerical examples involving single and multiple inclusions/holes in 3-D with different configurations. The obtained numerical results are compared with reference solutions based on analytical and standard non-adaptive XFEM methods.

© 2016 Elsevier Ltd. All rights reserved.

## 1. Introduction

The so-called weak discontinuities such as voids and inclusions greatly affect the integrity and performance of structures or components. Accurate modeling of such discontinuities is of interest to the researchers and scientists. In order to evaluate the mechanical behavior, major discontinuities in the components must be fully considered. High gradients are often encountered at the vicinity of discontinuities, in which fine-scale meshes around the discontinuities are often required to improve the final outputs of the solutions. However, the amount of computational time required may be very huge if fine-scale meshes are applied to the whole structure or the body (in some particular cases, the computations may even be failed). To reduce the computational effort, the fine-scale meshes around the discontinuities are often preferred, while the

coarse-scale meshes are utilized for the regions far from the discontinuities. Consequently, two major issues arisen from that approach must be taken into account: (1) how to define the domain discretized with fine-scale meshes; and (2) how to link/couple the mismatching problem between different scales of the meshes.

About the fine-scale mesh domain, there are two ways that are often used to determine the region discretized by the fine-scale mesh. The first is that the domain is defined in advance, the easy implementation is the advantage of this way, but the domain determined is based upon the experience of the analysts. This way is in general not suited to practical problems. The other is that the region discretized by the fine-scale mesh is performed with the aid of adaptive strategies, i.e., the elements that have a relative error greater than a specified tolerance value are refined. The region is automatically determined by the error analysis, so the second approach is more reasonable and highly suitable for practices. As linking the mismatch of different mesh-scales, some special techniques have been developed and available in literature such as the Lagrange multipliers [1], the projection method [2], the penalty function parameters [3], the mortar method [4], and the Arlequin

\* Corresponding author at: Duy Tan University, Vietnam.

\*\* Corresponding author at: Hohai University, China.

E-mail addresses: [tiantangyu@hhu.edu.cn](mailto:tiantangyu@hhu.edu.cn) (T. Yu), [buiquocinh@duytan.edu.vn](mailto:buiquocinh@duytan.edu.vn), [tinh.buiquoc@gmail.com](mailto:tinh.buiquoc@gmail.com) (T.Q. Bui).

method [5]. From the implementation point of view, these methods however often require some modifications on the system matrix, leading to a complicated implementation.

The extended finite element method (XFEM) is becoming popular for modeling arbitrary discontinuities because the geometry of discontinuities is independent of the finite element mesh, see for instance [6,7]. The basic idea behind the XFEM is that the standard finite element approximation is enriched with some special functions around the discontinuities in the framework of partition of unity. In the past over decades, a large number of studies have been conducted to improve or apply the original XFEM for various configurations and problems, e.g., see [7–21]. Kang et al. [15] proposed an enhanced XFEM based on consecutive-interpolation procedure for accurately extracting crack-tip fields in two-dimensional solids. Pathak et al. [22] proposed a simple and efficient XFEM approach for 3-D cracks. A crack front is divided into a number of piecewise curve segments to avoid an iterative solution. In crack front elements, the level set functions are approximated by higher order shape functions which assure the accurate modeling of the crack front. Later, the method is further applied to model fatigue crack growth simulations of 3-D problems [23, 24]. Pathak et al. [25,26] simulated fatigue crack growth simulations of bi-material interfacial cracks using XFEM under elastic loading and thermo-elastic loading. The material interface is modeled by a signed distance function whereas a crack is modeled by Heaviside and asymptotic crack tip enrichment functions. Singh et al. [27] evaluated the fatigue life of homogeneous plate containing multiple discontinuities (holes, minor cracks and inclusions) by XFEM under cyclic loading condition, and investigated the effect of the minor cracks, voids and inclusions on the fatigue life of the material in detail.

Nevertheless, one must be noted that adaptive XFEM or local mesh refinement XFEM developed for solving discontinuous problems like cracks or curved interface in two-dimensional (2-D) can be found in literature, see for instance [28–33]. In Ref. [29], the error estimator is based on a stress smoothing technique. The advantage of stress recovery is that it can be easily extended to generally inelastic material behavior. The incorporation of microstructural features is obtained by using the multiscale projection method. In Ref. [30], the existing singlescale crack propagation and crack coalescence methods are coupled to the multiscale projection method. In Ref. [32], the different scales are linked by using a local multi-grid approach, whereas the refined domain is defined by the user at the beginning of the simulation. However, preceding works in terms of adaptive XFEM devoted to inclusions and voids modeling are rather rare, especially three-dimensional (3-D) cases. In fact, accurate modeling of 3-D inclusions and voids structures, for instance, in composite reinforced materials, remains a challenging task in the computational mechanics.

The novelty, also the main objective, of this contribution is that a novel adaptive extended finite element method, which is later termed as A-XFEM for the sake of brevity, is developed, particularly devoting to the accurate modeling of weak discontinuous problems such as inclusions and voids in 3-D solids. We aim at offering higher accuracy of the solutions using our A-XFEM as compared with that of the standard XFEM but with a significant less number of degrees of freedom of the system. In other words, the computational time in modeling 3-D inclusions and voids problems is reduced significantly by using the developed A-XFEM, illustrating the effectiveness of the present approach over the standard non-adaptive one. To this end, the present formulation is an adaptive method based on a *posteriori* error estimation scheme driven by a recovery strain procedure. In order to treat both the discontinuity in the field variables and the mismatch of different mesh-scales, the local enriched partition-of-unity method and the variable-node hexahedron elements based on the generic point interpolation are hence rigorously integrated into the formulation.

The elements, which have been detected by a *posteriori* error estimation algorithm, are refined in the adaptive procedure. In this work, the adaptive procedure using a *posteriori* error estimation in terms of the XFEM is adopted [34,28–30]. The Zienkiewicz and Zhu error estimator [35] is used and that is based on a strain smoothing technique. The enhanced or smoothed strains incorporating with the discontinuities induced by interfaces are recovered, by which the error estimation for arbitrary distributed interfaces can be made. An error indicator that is applied to subsequently refined meshes is gained with a relative error, and every element with a relative error exceeds a given specified value of tolerance error is then refined with a set of subdivision elements.

The variable-node elements recently reported in [36,37] are introduced in this work. The variable-node elements have an arbitrary number of nodes on the element side and face, the mismatching interfaces are converted into matching interfaces in a straightforward manner, provided that the system matrix does not need to be modified.

One of the main advantages of the proposed A-XFEM is that it enables one to utilize a refinement mesh only in the vicinity of the discontinuity where it is required by means of an automatic mesh refinement algorithm, and the matching interfaces between different mesh-scale are directly obtained. It is worth noting that the traditional fixed-node element is one special case for the variable-node elements, hence the variable-node hexahedron elements can be implemented within existing XFEM computer codes with little modification and effort. The A-XFEM associated with an adaptive process allows the users to achieve desired accuracies with some trials.

In this paper, we restrict our interest by studying the problems under static situation only, focusing on the demonstration of the applicability and performance of the developed A-XFEM in simulation of 3-D inclusions and voids.

The paper is structured as follows. The novel 3-D A-XFEM formulation is presented in Section 2, in which we detail the variable-node hexahedron elements to link different scale elements, a *posteriori* recovery-based error estimator for the adaptive purpose, numerical integration, enriched displacement approximations, etc. Four representative numerical examples of single and multiple inclusions are considered and presented in Section 3, while Section 4 shows the numerical results of single and multiple voids/holes. Some conclusions drawn from the study are given in Section 5.

## 2. Three-dimensional adaptive XFEM formulation for weak discontinuities

### 2.1. XFEM approximation of field variables

The enriched displacement field can be expressed in the following form [34,38,39]:

$$\mathbf{u}^h(\mathbf{x}) = \sum_{i \in \mathbf{I}} \mathbf{u}_i N_i(\mathbf{x}) + \sum_{j \in \mathbf{J}} \mathbf{a}_j N_j(\mathbf{x}) \Psi(\mathbf{x}) \quad (1)$$

where  $N_i(\mathbf{x})$  and  $N_j(\mathbf{x})$  are the standard shape functions;  $\mathbf{u}_i$  and  $\mathbf{a}_j$  are the displacement and enrichment nodal variables, respectively;  $\Psi(\mathbf{x})$  represents the enrichment function which depends on the type of problem;  $\mathbf{I}$  is the set of all nodes in the discretization, while  $\mathbf{J}$  is the set of nodes whose support is intersected by the discontinuity. In Eq. (1), the first term denotes the classical finite element approximation whereas the second term represents the enrichment function considered in the XFEM.

For inclusions modeling, the enrichment function is chosen as [38]

$$\psi(\mathbf{x}) = \sum_I |\varphi_I| N_I(\mathbf{x}) - \left| \sum_I \varphi_I N_I(\mathbf{x}) \right| \quad (2)$$

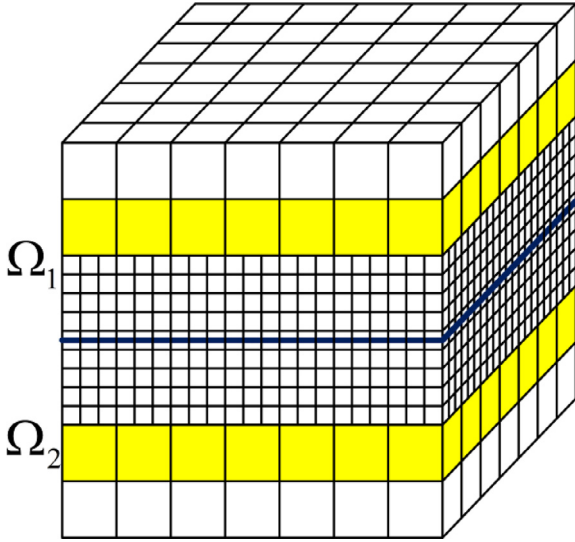


**Fig. 1.** Schematic of hexahedral meshes discretization of a laminate containing two different scale hexahedron elements. One layer of variable-node hexahedron elements (marked in yellow) is defined to link two different meshes. The blue solid line represents the interface. (For interpretation of the references to color in this figure legend, the reader is referred to the web version of this article.)

with  $\varphi_l$  indicates the nodal value of the level set function.

For voids or holes modeling, the displacement field is alternatively approximated by [39]:

$$\mathbf{u}^h(\mathbf{x}) = \sum_{i \in I} N_i(\mathbf{x}) \bar{H}(\mathbf{x}) \mathbf{u}_i \quad (3)$$

where

$$\bar{H}(\mathbf{x}) = \begin{cases} 1 & \mathbf{x} \in \Omega \\ 0 & \mathbf{x} \notin \Omega \end{cases} \quad (4)$$

## 2.2. Coupling meshes: variable-node hexahedron element based on the point interpolation

We adopt the variable-node hexahedron elements based on the point interpolation to couple different mesh-scales [36,37]. Fig. 1 schematically depicts one layer of variable-node hexahedron elements marked in yellow. Note that this class of elements are also known as transition elements, which link elements involving different scales. Major advantages must be stressed out here that, unlike the classical existing transition elements, the number of nodes on the element faces of the adopted variable-node hexahedron elements can be arbitrary, provided that special bases are employed that have slope discontinuities in 3-D domains. More importantly, the elements defined in such a way retain the linear interpolation between any two neighboring nodes. In [36,37], the variable-node elements have proven to be capable of offering a flexible way to resolve the non-mismatching mesh problems (i.e., the mesh connection and adaptive mesh refinement).

The displacements  $\mathbf{u}^h(\xi)$  approximated for  $\mathbf{u}(\xi)$  by the point interpolation, with  $N_p$  based-polynomials, are given by

$$\mathbf{u}^h(\xi) = \sum_{i=1}^{N_p} N_i(\xi) \mathbf{u}_i = \mathbf{a}^T \mathbf{p}(\xi) \quad (5)$$

in which  $N_p$  defines the number of sampling points in the point interpolation. The shape function  $N_i$  that is associated with node  $i$  is defined by

$$N_i = \begin{bmatrix} N_i & 0 & 0 \\ 0 & N_i & 0 \\ 0 & 0 & N_i \end{bmatrix} \quad (6)$$

where  $\mathbf{u}_i = [u_i \ v_i \ w_i]^T$  is the nodal variable vector;  $\mathbf{p}(\xi)$  is the  $N_p \times 1$  column vector of the polynomial basis, while  $\mathbf{a}^T$  is the  $3 \times N_p$  matrix of the unknown coefficients.

In this work, the polynomial basis used for the eight-node hexahedron element is

$$\mathbf{p}(\xi) = [1 \ \xi \ \eta \ \zeta \ \xi \eta \ \eta \zeta \ \xi \zeta \ \xi \eta \zeta]^T \quad (7)$$

with  $\xi$ ,  $\eta$  and  $\zeta$  being the local coordinates in the isoparametric element.

The point interpolation can then be expressed as

$$\mathbf{u}^h(\xi) = \mathbf{a}^T \mathbf{p}(\xi) = \mathbf{U}^T \mathbf{q}^{-1} \mathbf{p}(\xi) \quad (8)$$

with

$$\mathbf{q} = [\mathbf{p}_1 \ \dots \ \mathbf{p}_8] \quad (9)$$

$$\mathbf{U}^T = [\mathbf{u}_1 \ \dots \ \mathbf{u}_8] \quad (10)$$

Based on the descriptions of Eqs. (5)–(10), we can derive the shape functions of the eight-node hexahedron element, which are written in general form as follows:

$$N_i(\xi) = \frac{1}{8} (1 + \xi \xi_i) (1 + \eta \eta_i) (1 + \zeta \zeta_i) \quad (11)$$

The variable-node hexahedron elements are then generated by adding some extra special basis to meet the point interpolation characteristics. It must be noted that the choice for the extra special basis generally depends upon the interpolation type required on the element-surfaces. All nodes of a linear variable-node hexahedron element (named as a  $(8+j+k+l+p+q+r)$ -node element) can be divided into 7 types, which are schematically depicted in Fig. 2:

- Type #1: 8 corner nodes of the hexahedron element;
- Type #2:  $j$  nodes on the edges of  $\xi = \pm 1$ ,  $\eta = \pm 1$ , and  $\zeta \neq \pm 1$ ;
- Type #3:  $k$  additional nodes on the edges of  $\eta = \pm 1$ ,  $\zeta = \pm 1$ , and  $\xi \neq \pm 1$ ;
- Type #4:  $l$  additional nodes on the edges of  $\xi = \pm 1$ ,  $\zeta = \pm 1$ , and  $\eta \neq \pm 1$ ;
- Type #5:  $p$  additional nodes on the surfaces of  $\xi = \pm 1$ ;
- Type #6:  $q$  additional nodes on the surfaces of  $\eta = \pm 1$ ; and
- Type #7:  $r$  additional nodes on the surfaces of  $\zeta = \pm 1$ .

Finally, the polynomial basis can be given by

$$\begin{aligned} \mathbf{p}(\xi) = & [1, \xi, \eta, \zeta, \xi \eta, \eta \zeta, \xi \zeta, \xi \eta \zeta, \\ & (\xi + \text{sign}(\xi_9))(\eta + \text{sign}(\eta_9))|\zeta - \zeta_9|, \dots, \\ & (\xi + \text{sign}(\xi_{8+j}))(\eta + \text{sign}(\eta_{8+j}))|\zeta - \zeta_{8+j}|, \\ & |\xi - \xi_{8+j+1}|(\eta + \text{sign}(\eta_{8+j+1}))(\zeta + \text{sign}(\zeta_{8+j+1})), \dots, \\ & |\xi - \xi_{8+j+k}|(\eta + \text{sign}(\eta_{8+j+k}))(\zeta + \text{sign}(\zeta_{8+j+k})), \\ & (\xi + \text{sign}(\xi_{8+j+k+1}))|\eta - \eta_{8+j+k+1}| \\ & (\zeta + \text{sign}(\zeta_{8+j+k+1})), \dots, (\xi + \text{sign}(\xi_{8+j+k+l})) \\ & |\eta - \eta_{8+j+k+l}|(\zeta + \text{sign}(\zeta_{8+j+k+l})), \\ & (\xi + \text{sign}(\xi_{8+j+k+l+1}))|\eta - \eta_{8+j+k+l+1}| \\ & |\zeta - \zeta_{8+j+k+l+1}|, \dots, (\xi + \text{sign}(\xi_{8+j+k+l+p})) \\ & |\eta - \eta_{8+j+k+l+p}| |\zeta - \zeta_{8+j+k+l+p}|, \\ & |\xi - \xi_{8+j+k+l+p+1}|(\eta + \text{sign}(\eta_{8+j+k+l+p+1})) \\ & |\zeta - \zeta_{8+j+k+l+p+1}|, \dots, |\xi - \xi_{8+j+k+l+p+q}| \\ & (\eta + \text{sign}(\eta_{8+j+k+l+p+q})) |\zeta - \zeta_{8+j+k+l+p+q}|, \\ & |\xi - \xi_{8+j+k+l+p+q+1}| |\eta - \eta_{8+j+k+l+p+q+1}| \\ & (\zeta + \text{sign}(\zeta_{8+j+k+l+p+q+1})), \dots, |\xi - \xi_{8+j+k+l+p+q+r}| \end{aligned}$$

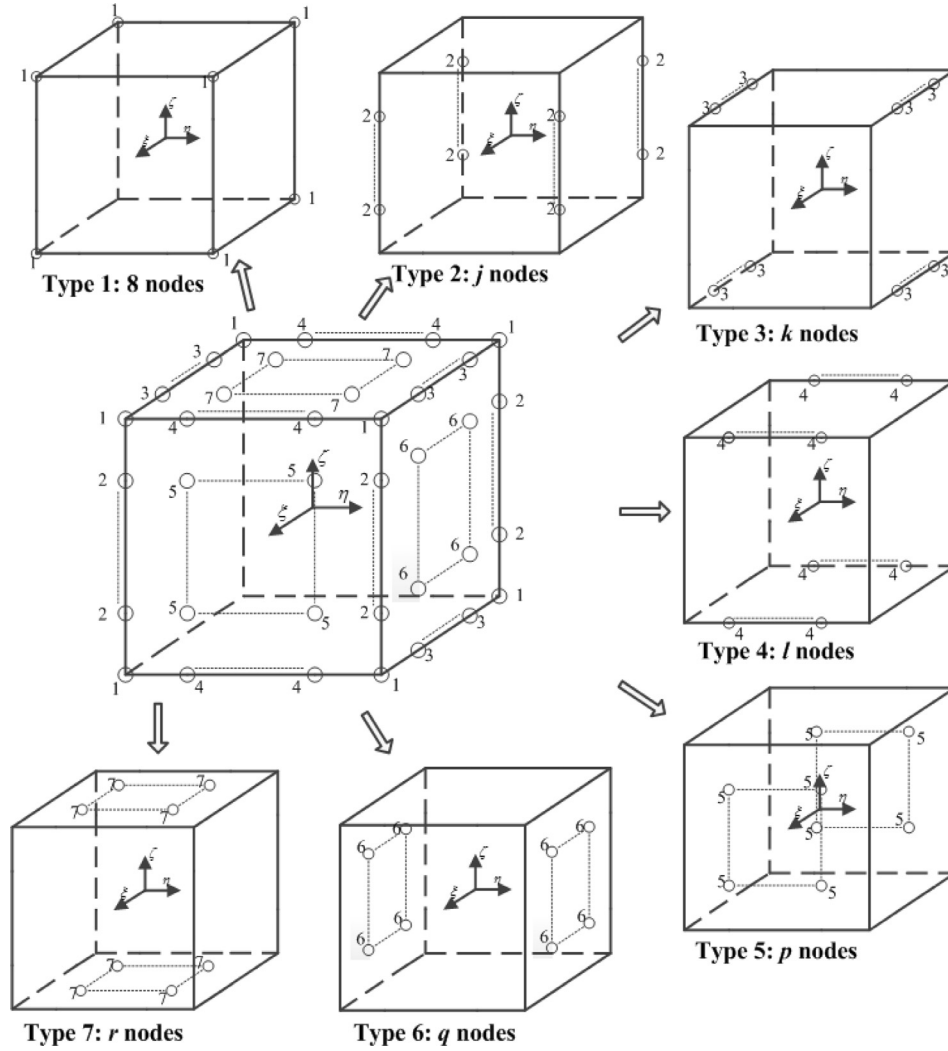


Fig. 2. Schematic representation of a  $(8 + j + k + l + p + q + r)$ -node element forming seven types of different grouped nodes.

$$|\eta - \eta_{8+j+k+l+p+q+r}|(\zeta + \text{sign}(\zeta_{8+j+k+l+p+q+r}))^T \quad (12)$$

The corresponding  $\mathbf{q} = \mathbf{p}(\xi_i)$  and  $\mathbf{U}^T$  are

$$\mathbf{U}^T = [\mathbf{u}_1 \dots \mathbf{u}_i \dots \mathbf{u}_{8+j+k+l+p+q+r}] \quad (13)$$

Based on Eq. (8), the shape functions of a  $(8 + j + k + l + p + q + r)$ -node element can be obtained as

$$[N_1, \dots, N_{8+j+k+l+p+q+r}]^T = \mathbf{q}^{-1} \mathbf{p}(\xi) \quad (14)$$

For more clearly, the shape functions of a typical 3-D variable 13-node hexahedron element are schematically shown in Fig. 3. One must be noted that the shape functions at each node possess the Kronecker's delta function property. In addition, variable-node element meets the following properties [37]: (1) partition of unity, (2) linear completeness at the element domain, and (3) at least piecewise linear interpolation between two neighboring nodes at all element boundaries.

### 2.3. Adaptive mesh refinement procedure: recovery based error estimator

An error estimator in the framework of an adaptive mesh refinement procedure must be defined to detect elements, which are then refined in the subsequent steps of refinements. It is accomplished based on an error indicator whose determinable relative errors exceed a specific tolerance.

#### 2.3.1. Recovery of the strain fields

The recovery-based error estimator can be revised according to the Zienkiewicz–Zhu error estimator [35]. The smoothed strains are recovered in a way by projecting the element strains onto the nodes, and by interpolating the nodal strains with the same ansatz functions that are employed for the calculation of the displacement fields.

Basically, the strains across the interface between two materials are discontinuous, so the enhanced or smoothed strain field for 3-D inclusions may be expressed as

$$\boldsymbol{\varepsilon}^s(\mathbf{x}) = \sum_{i \in N^s} N_i(\mathbf{x}) \mathbf{d}_i + \sum_{j \in N^{\text{cut}}} N_j(\mathbf{x}) [H(\mathbf{x}) - H(\mathbf{x}_j)] \mathbf{e}_j \quad (15)$$

where  $\mathbf{d}_i$  and  $\mathbf{e}_j$  reflect the nodal degree of freedoms of the enhanced strains;  $H(\mathbf{x})$  is a modified Heaviside step function which takes on the value +1 at one side of the interface and -1 at another side of the interface.

The coefficients  $\mathbf{d}_i$  and  $\mathbf{e}_j$  can be evaluated by minimizing the square of the  $L_2$  norm of the difference between the XFEM based computed strain field and the smoothed strain field over the whole domain, i.e.,

$$\int_{\Omega} \|\boldsymbol{\varepsilon}^s - \boldsymbol{\varepsilon}\|^2 d\Omega \rightarrow \min \quad (16)$$

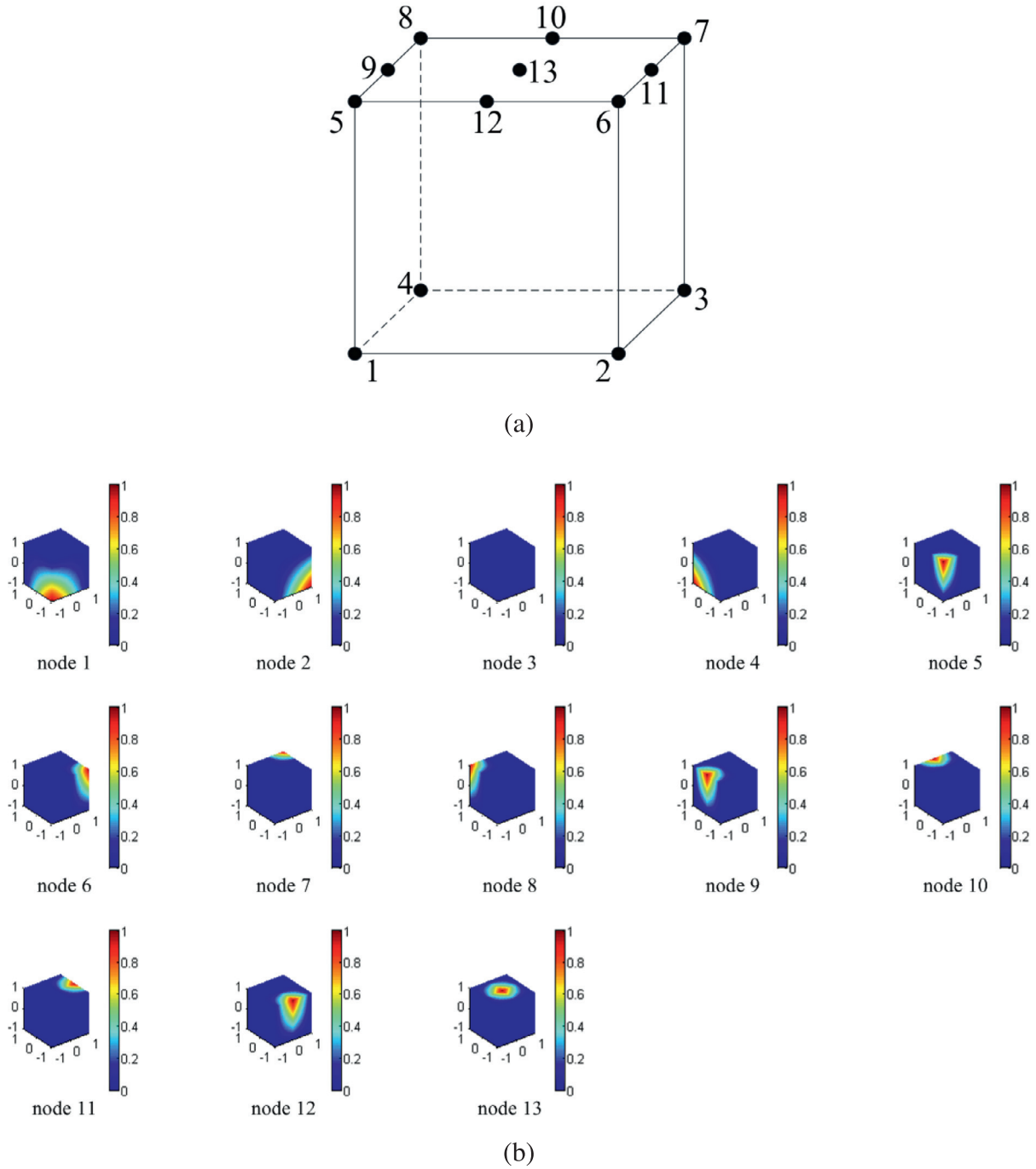


**Fig. 3.** The shape functions of a typical 3-D variable 13-node hexahedron element: The element (a) and its representative shape functions possessing the Kronecker's delta function property at each node (b).

where  $\boldsymbol{\epsilon} = [\epsilon_x \ \epsilon_y \ \epsilon_z \ \gamma_{xy} \ \gamma_{xz} \ \gamma_{yz}]^T$  is the strain vector obtained through the XFEM.

From Eq. (16), one can obtain the following linear equation system

$$\mathbf{A}\boldsymbol{\epsilon}^* = \mathbf{C} \quad (17)$$

where  $\boldsymbol{\epsilon}^* = [\mathbf{d} \ \mathbf{e}]^T$  is the vector of the nodal unknowns in the smoothed strain field, while  $\mathbf{A}$  and  $\mathbf{C}$  respectively are the coefficient matrix and nodal coefficient vector.

The element contribution to matrix  $\mathbf{A}$  is

$$\mathbf{a}_{ij} = \begin{bmatrix} \mathbf{a}_{ij}^{dd} & \mathbf{a}_{ij}^{de} \\ \mathbf{a}_{ij}^{ed} & \mathbf{a}_{ij}^{ee} \end{bmatrix} \quad (18)$$

where

$$\mathbf{a}_{ij}^{rs} = \int_{\Omega_e} (\mathbf{B}_i^r)^T \mathbf{B}_j^s d\Omega; \quad (r, s = d, e) \quad (19)$$

with

$$\mathbf{B}_i^d = \begin{bmatrix} N_i & 0 & 0 & 0 & 0 & 0 \\ 0 & N_i & 0 & 0 & 0 & 0 \\ 0 & 0 & N_i & 0 & 0 & 0 \\ 0 & 0 & 0 & N_i & 0 & 0 \\ 0 & 0 & 0 & 0 & N_i & 0 \\ 0 & 0 & 0 & 0 & 0 & N_i \end{bmatrix} \quad (20)$$

$$\mathbf{B}_i^e = [H(\mathbf{x}) - H(\mathbf{x}_i)] \begin{bmatrix} N_i & 0 & 0 & 0 & 0 & 0 \\ 0 & N_i & 0 & 0 & 0 & 0 \\ 0 & 0 & N_i & 0 & 0 & 0 \\ 0 & 0 & 0 & N_i & 0 & 0 \\ 0 & 0 & 0 & 0 & N_i & 0 \\ 0 & 0 & 0 & 0 & 0 & N_i \end{bmatrix} \quad (21)$$

Additionally, the element contribution to  $\mathbf{C}$  is

$$\mathbf{c}_i = [\mathbf{c}_i^d \ \mathbf{c}_i^e] \quad (22)$$

with

$$\mathbf{c}_i^d = \int_{\Omega_e} \mathbf{B}_i^d \boldsymbol{\varepsilon} d\Omega \quad (23)$$

$$\mathbf{c}_i^e = \int_{\Omega_e} \mathbf{B}_i^e \boldsymbol{\varepsilon} d\Omega \quad (24)$$

The enhanced or smoothed strain field for void or hole problem can be expressed as

$$\boldsymbol{\varepsilon}^s(\mathbf{x}) = \sum_{i \in N^s} N_i(\mathbf{x}) \bar{H}(\mathbf{x}) \mathbf{d}_i \quad (25)$$

where  $\mathbf{d}_i$  reflects the nodal degree of freedoms of the enhanced strains.

2.3.2. Error estimator

The  $L_2$  norm error of the strains for element  $i$  is calculated by

$$\text{err}(i) = \sqrt{\frac{1}{\Omega_e} \int_{\Omega_e} (\boldsymbol{\varepsilon} - \boldsymbol{\varepsilon}^s)^T (\boldsymbol{\varepsilon} - \boldsymbol{\varepsilon}^s) d\Omega} \quad (26)$$

with  $\Omega_e$  is the area of the element.

The maximum  $L_2$  norm strain of the elements is  $\text{err}_{\max}$ , then the relative error for element  $i$  is estimated as follows:

$$\eta(i) = \frac{\text{err}(i)}{\text{err}_{\max}} \times 100\% \quad (27)$$

The  $L_2$  norm error of the strains for the whole domain is finally calculated by

$$\text{err}_{\text{Total}} = \sqrt{\int_{\Omega} (\boldsymbol{\varepsilon} - \boldsymbol{\varepsilon}^s)^T (\boldsymbol{\varepsilon} - \boldsymbol{\varepsilon}^s) d\Omega} \quad (28)$$

The  $L_2$  norm error of the displacements for the whole domain is calculated by

$$\text{err}_{\text{Total}} = \sqrt{\int_{\Omega} (\mathbf{u} - \mathbf{u}^s)^T (\mathbf{u} - \mathbf{u}^s) d\Omega} \quad (29)$$

where  $\mathbf{u}$  and  $\mathbf{u}^s$  are the numerical and exact displacement solutions, respectively.

2.4. Numerical integration of the A-XFEM

The present approach naturally owns different types of elements, which are mainly caused by interface geometry of inclusions and voids in the composites. The numerical integration to different elements is essential and that plays an important role to the success of the method. In words, the accuracy of the developed A-XFEM partially depends on the treatment procedure of the numerical integration. In fact, the issues pertaining to the accuracy and effectiveness of numerical integration in terms of XFEM/GFEM have been studied and addressed in several previous works, e.g., see [40–42]. The following integration schemes are fulfilled in the proposed method in order to make sure the strain field to be sufficiently integrated.

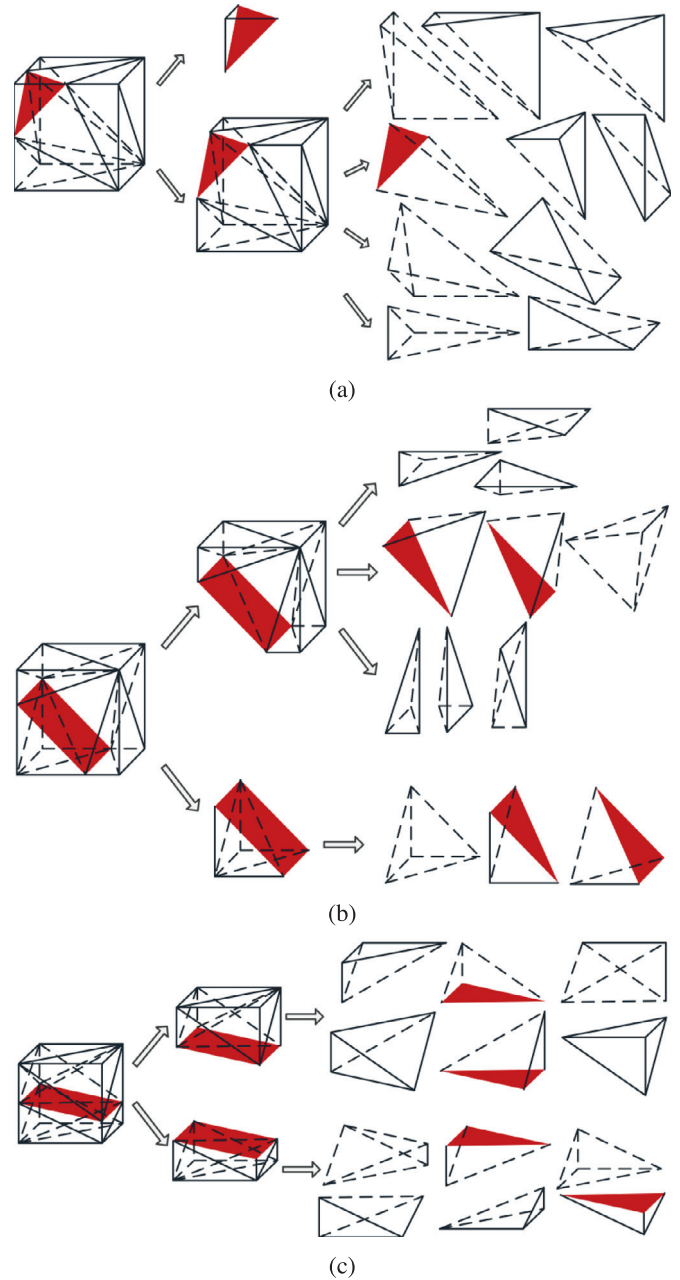
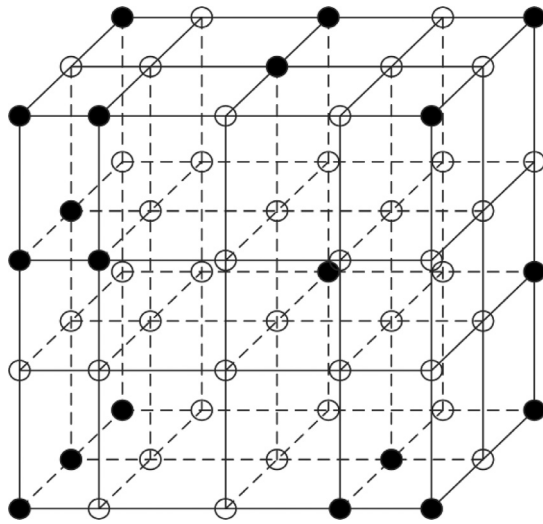


Fig. 4. Generation of sub-tetrahedrons for the quadrature: interface element (a) which is divided into a tetrahedron and a heptahedron by the interface; interface element (b) which is divided into a pentahedron and a heptahedron by the interface; and interface element (c) which is divided into two hexahedrons.

(1) *Eight-node hexahedron elements*: The second-order Gaussian quadrature scheme is taken to treat the numerical integration of the eight-node hexahedron elements that do not contain any enriched nodes. For the elements that involve enriched nodes (but are not interface elements), high-order Gaussian quadrature rule is applied to improve the accuracy of the output results instead. However, a special treatment of numerical integration for interface elements is needed. The treatment is carried out by partitioning the interface hexahedron element into sub-tetrahedrons, which are hence schematically depicted in Fig. 4, whose boundaries align with the interface geometry. Traditional Gauss quadrature rules are taken in sub-tetrahedrons.

Our own numerical experiments, which will be presented later in the numerical examples, are indicated that accuracy results can



**Fig. 5.** Schematically generating quadrature sub-domains for a regular variable-node hexahedron element which do not contain any discontinuities. The solid points represent the nodal points, while the hollow points represent the supplementary points.

be obtained by using the subdivision numerical integration, while the procedure of partitioning elements is complicated. Alternatively, a method to evaluate regular domain integrals without domain discretization in terms of meshfree method is presented [43]. The underlying principle of this integration technique is its simplicity and accuracy as a domain integral is transformed into a boundary integral and a 1D integral. The integration technique in [43] is interesting, and generally it could be integrated into the present formulation to further enhance its efficiency, avoiding the partitioning elements.

(2) *Variable-node hexahedron elements:* Treating the numerical integration for the variable-node hexahedron elements that contain no interface is briefly presented. Through Eq. (14), the nodal shape functions of the variable-node hexahedron elements are calculated, and their slope discontinuity may give rise to the problems of inter-subdomain boundaries. The sub-hexahedrons are thus generated to overcome the slope discontinuity in the numerical integration, where the shape functions still show the linear interpolation within a sub-hexahedron, see Fig. 5. The conventional second-order Gauss quadrature rule is then applied for those sub-hexahedrons.

(3) *Variable-node interface hexahedron elements:* In some particular cases and once the mesh is refined subsequently by more than one step of refinement, it could be happened that the variable-node transition hexahedron elements may become interface elements. In such circumstance, a special treatment of the numerical integration of variable-node interface elements is necessary to be made. Sub-division of the interface variable-node hexahedron element is utilized as schematically represented in Fig. 6, and sub-hexahedrons are then obtained. These sub-hexahedrons can then be divided into 4 types:

- Type #1: elements that are like interface (a), denoted by the term “(a)”;
- Type #2: elements that are like interface (b), denoted by the term “(b)”;
- Type #3: elements that are like interface (c), denoted by the term “(c)”;
- Type #4: regular elements that do not contain any discontinuities.

Then, the Gauss quadrature scheme is used for the numerical integrations of those types of sub-elements.

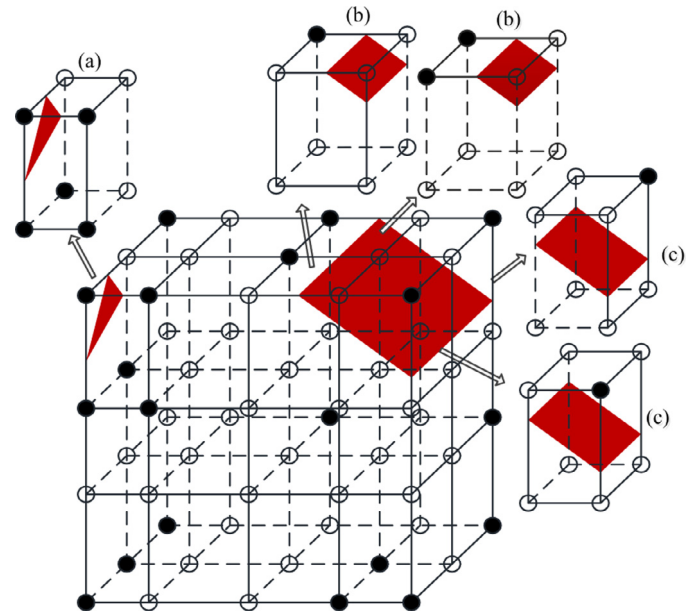


**Fig. 6.** Schematically generating quadrature sub-domains for a variable-node interface element: variable-node interface element (a), variable-node interface element (b), variable-node interface element (c). The solid points represent the nodal points, while the hollow points represent the supplementary points. The inter-surface is marked and filled in red.

Once again, the special treatment of the numerical integration in the present codes as described above is necessary since it is to ensure the convergence of the solutions or avoid some undesirable situations.

## 2.5. Numerical implementation

The main steps of solution procedure for the whole problem by using the proposed method are briefly presented here.

- (1) The problem domain is discretized with coarse-scale meshes, without considering the inclusion/void shape and location.
- (2) Loop over the number of refinement.
  - a. Enriched nodes are selected using the level set method.
  - b. Assemble the global stiffness matrix and load array.
  - c. Solve the governing equations considering the constraint conditions.
  - d. Calculate the smoothed strain field through Eq. (15) or Eq.(25).
  - e. Calculate the L2 norm error of the strains for each element through Eq. (26).
  - f. Calculate the relative error for each element through Eq. (27).
  - g. The elements in which the relative error exceeds the tolerance are refined.
- (3) Post-processing for the output of the computed results.

## 3. Numerical examples of single and multiple inclusions

In this section, numerical experiments of modeling single and multiple inclusions using the proposed A-XFEM are analyzed and discussed. Four representative numerical examples of 3-D single and multiple inclusions embedded in a matrix are hence considered and analyzed. All the numerical results are discussed and compared with analytical solutions and the conventional XFEM results using fine meshes to show the accuracy and effectiveness of the developed A-XFEM.

In all examples of inclusions, the material parameters set for the matrix  $\Omega_1$ : the Young's modulus  $E=1000$  GPa and the Pois-

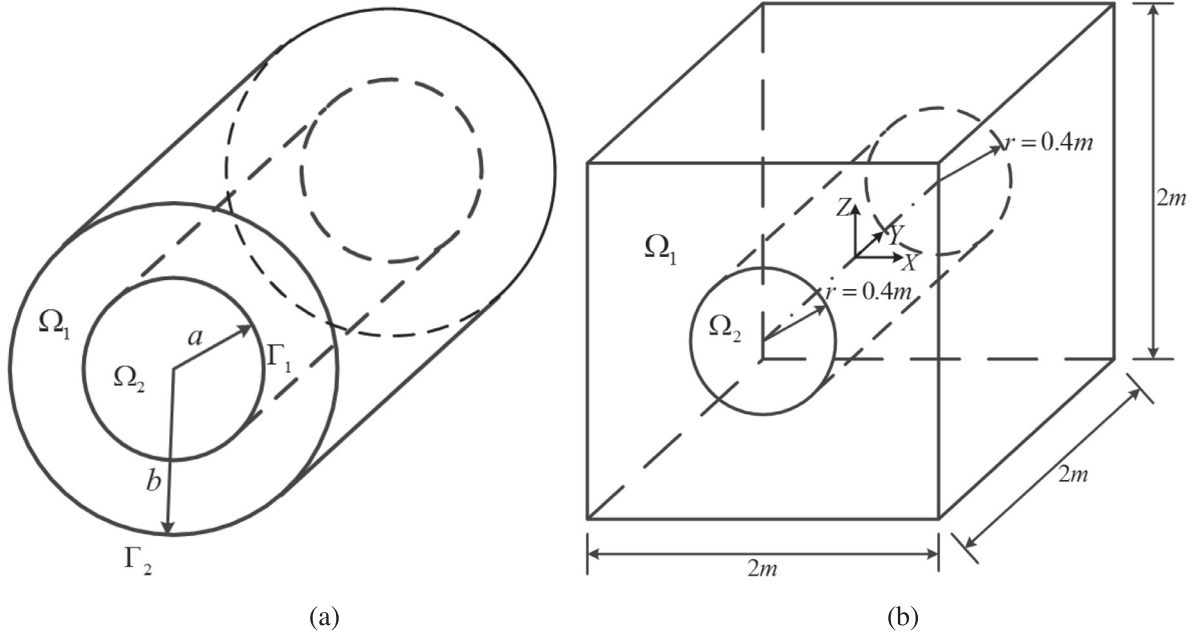


Fig. 7. Bimaterial boundary-value problem (a), geometric representation of a cube with a cylindrical inclusion and its configuration parameters (b).

son ratio  $\nu=0.3$ , and for the inclusion  $\Omega_2$ : the Young’s modulus  $E=1$  GPa and the Poisson ratio  $\nu=0.25$ .

3.1. A cylindrical inclusion

We start by considering an infinitely long cylinder composed of two different materials as shown in Fig. 7a. There is a discontinuity in the material constants across the interface  $\Gamma_1(r=a)$ . We impose the displacement field:  $u_r=r, u_\theta=0$  on the boundary  $\Gamma_2(r=b)$ . The exact displacement solution are given by [39]

$$u_r(r) = \begin{cases} [(1 - \frac{b^2}{a^2})\alpha + \frac{b^2}{a^2}]r, & 0 \leq r \leq a \\ (r - \frac{b^2}{r})\alpha + \frac{b^2}{r}, & a \leq r \leq b \end{cases} \quad (30a)$$

$$u_\theta = 0 \quad (30b)$$

where,  $\alpha = \frac{(\lambda_2 + \mu_1 + \mu_2)b^2}{(\lambda_1 + \mu_1)a^2 + (\lambda_2 + \mu_2)(b^2 - a^2) + \mu_1 b^2}$ ;  $\lambda_1$  and  $\mu_1$  are Lamé parameters in  $\Omega_1$ ;  $\lambda_2$  and  $\mu_2$  are Lamé parameters in  $\Omega_2$ .

In the numerical model, we consider a cube of  $2m \times 2m \times 2m$  with a cylindrical inclusion ( $\Omega_2$ ) of a radius  $a=0.4$  m, depicted in Fig. 7b. Regarding the boundary conditions, on the top and bottom and left and right faces of the cube, the exact displacements using Eq. (30) are imposed ( $a=0.4$  mand  $b=2.0$  m), and on the front and back faces of the cube, the normal displacements vertical to the face are set equal to zero. The origin of coordinate system locates at the center of the cube, as shown in Fig. 7b.

The displacement  $L_2$  norm is then estimated for each step of refinement using the A-XFEM and is compared with the results derived from the conventional XFEM. The study is to show the accuracy of the developed A-XFEM in 3-D inclusions.

In this example, a tolerance error of 5% is taken. Through the proposed adaptive mesh refinement procedure, the elements which have a relative error greater than the specified tolerance error are refined with more sub-elements. This task means that an eight-node hexahedron element (parent element) has been detected and is then sub-divided into some sub-elements (children elements). Notice that the number of children elements can be arbitrary in the present formulation. Our numerical experiments have found that a refinement with a set of  $3 \times 3 \times 3$  children elements can offer good results, and this set is used throughout the study unless stated otherwise.

Fig. 8a shows an initial mesh of  $6 \times 6 \times 6$  elements of a cube generated by the A-XFEM as its initial step of refinement. We apply the adaptive algorithm based on error estimator, and thus all the discretized elements of the domain of interest are detected, and then a set of elements around the interface are selected and labeled. To this end, the elements detected are those that will be refined in the next refinement. The initial mesh in Fig. 8a is now refined, by using  $2 \times 2 \times 2$  sub-elements and  $3 \times 3 \times 3$  sub-elements, the corresponding two refined meshes are obtained and depicted in Fig. 8b and c, respectively.

For comparison, results conducted by using the conventional XFEM are added. To this end, Figs. 8d and 8e thus show the entire computational domain using small-scale elements of  $12 \times 12 \times 12$  elements and  $18 \times 18 \times 18$  elements. All the meshes in Fig. 8 are interesting since the main feature and the advantages of the present A-XFEM over the non-adaptive XFEM is illustrated. It clearly reveals that the refined mesh is only to be dealt with for the region that covers the interface, and more importantly the regions far from the discontinuous region, the interface, are not taken into account. It must be mentioned here that the number of elements or nodes gained by the non-adaptive XFEM are much larger than that discretized by the A-XFEM. This issue is discussed in the following numerical results.

For convenience in the representation of the numerical results, we pick points in  $y = 0, z = 0, x = 0.3 \text{ m} \sim 0.7 \text{ m}$  to calculate their  $x$ -direction displacement. Fig. 9 represents the calculated  $x$ -direction displacement results in  $y = 0, z = 0, x = 0.3 \text{ m} \sim 0.7 \text{ m}$  using the A-XFEM and the non-adaptive XFEM with a fine mesh. It can be observed in Fig. 9 that the two refined numerical results of the displacement gained by the A-XFEM are in good agreement with those derived from the standard non-adaptive XFEM with the fine mesh, and are closer to the exact displacements than those from the initial mesh. The initial mesh, not surprisingly, yields poor results. This exactly reflects the desirable characteristics of the present A-XFEM. However, the finer mesh is taken the more expensive the higher computational time of the conventional XFEM is required, which is not suited for practices. Definitely, the efficiency of a method is an important factor that ones must take into account in their realistic works. The adaptive refinement methods, in this way, and like the one being studied, are preferable. Fig. 10 shows the von Mises stress contours computed by using the

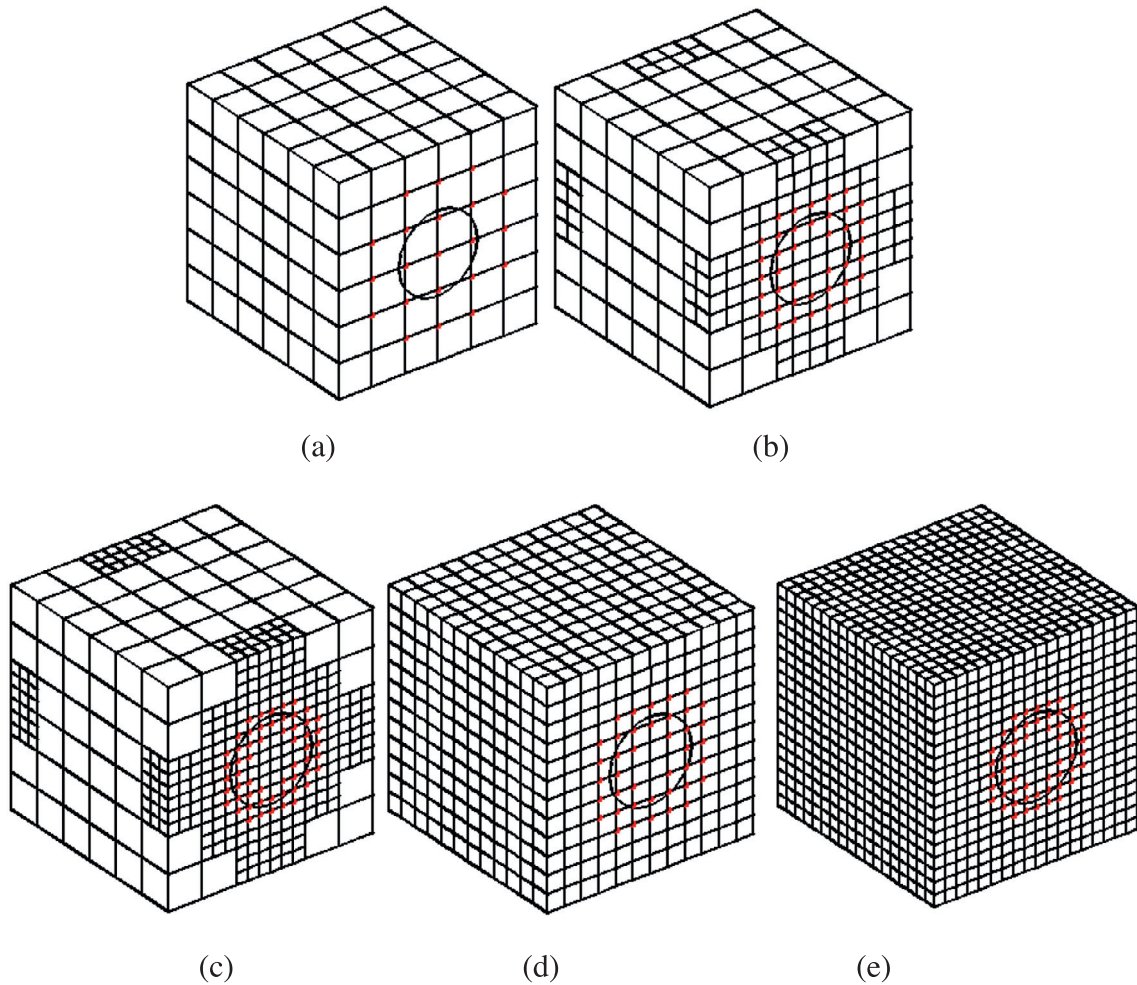


**Fig. 8.** A cube with a cylindrical inclusion: initial mesh (a); the refined A-XFEM mesh (using  $2 \times 2 \times 2$  sub-elements) (b); the refined A-XFEM mesh (using  $3 \times 3 \times 3$  sub-elements) (c); the conventional XFEM using  $12 \times 12 \times 12$  elements (d) and the conventional XFEM using  $18 \times 18 \times 18$  elements (e).

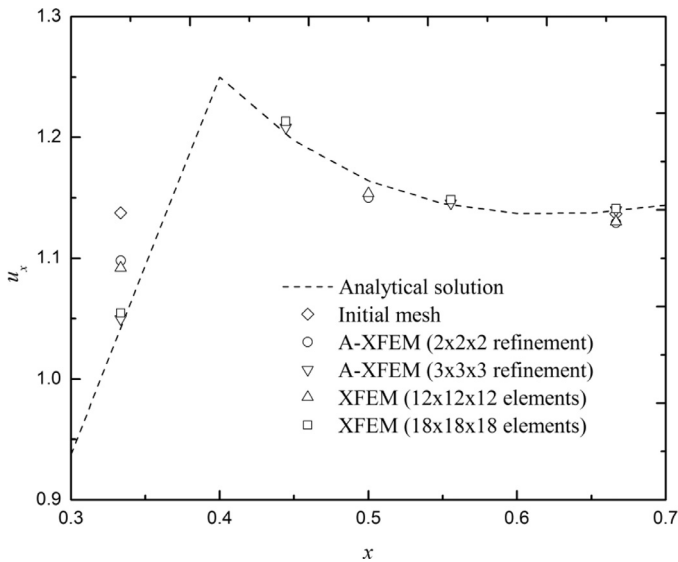


**Fig. 9.** Comparison of the  $x$ -direction displacement in  $y = 0, z = 0, x = 0.3 \text{ m} \sim 0.7 \text{ m}$  for a cube with a cylindrical inclusion among the A-XFEM, the conventional XFEM and the exact solution.

A-XFEM with different refinements and the conventional XFEM with fine mesh. The stress distribution obtained from both methods is reasonable and they agree between each other. We here typ-

ically show the stresses for the initial and the first step of refinement, and of course stresses by further refinements can also be gained in such a way.

The number of discretized elements through the A-XFEM reported in Table 1 is much less than that by the non-adaptive counterpart, reflecting the advantages of the A-XFEM. Also, this feature makes the method to be an ideal candidate for practical applications. Table 1 presents the strain  $L_2$  norm error, Eq. (28), calculated by the A-XFEM and the common XFEM. The number of DOFs and the strain  $L_2$  norm error reported clearly illustrate a better performance of the developed A-XFEM over the non-adaptive XFEM. Compared with the conventional XFEM, the proposed A-XFEM not only offers higher accuracy on the results, but also performs less number of DOFs (i.e., the computational time can also be reduced).

*Remark #1:* A given tolerance error has been used in all the computations so far. From the theoretical point of view, the smaller the tolerance is employed the better the results could be obtained. From the numerical implementation point of view, the smaller the tolerance is taken the higher the computational cost could be reached. Therefore, the cost must be a critical factor for the selection of this tolerance error in practice. The tolerance error for a given problem in general can be straightforwardly determined. It can be attempted to, for instance, through numerical experiments using the A-XFEM. In fact, the accuracy of the output is controllable, due to the adaptive algorithm. Nevertheless, we have found from this study that the value of the tolerance error may be problem-dependent, but its determination is trivial.

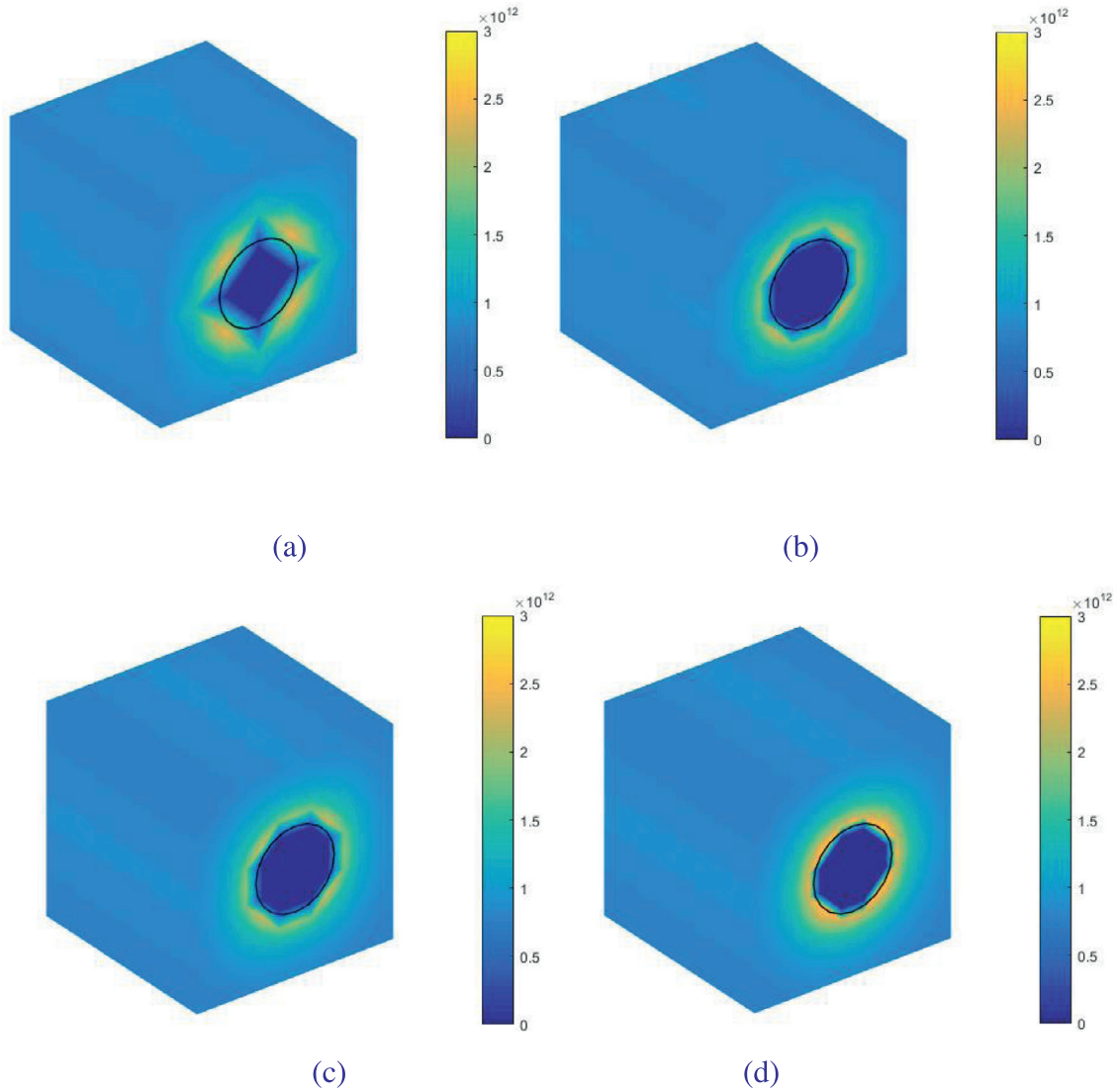


**Fig. 10.** Distribution of the von Mises stress contours for a cube with a cylindrical inclusion: (a) initial mesh; (b) the refined A-XFEM mesh using  $2 \times 2 \times 2$  sub-elements; (c) the refined A-XFEM mesh using  $3 \times 3 \times 3$  sub-elements; (d) conventional XFEM using  $18 \times 18 \times 18$  elements.

**Table 1**

The displacement and strain  $L_2$  norm obtained by the A-XFEM for different refinement methods. The conventional XFEM results are also added for the comparison purpose.

	Initial mesh	A-XFEM ( $2 \times 2 \times 2$ refinement)	A-XFEM ( $3 \times 3 \times 3$ refinement)	XFEM ( $12 \times 12 \times 12$ elements)	XFEM ( $18 \times 18 \times 18$ elements)
DOFs	343	1413	4003	2197	6859
Displacement $L_2$ norm error	0.38157	0.10254	0.04187	0.10222	0.04181
Strain $L_2$ norm error ( $\times 10^{-6}$ )	2.72996	0.81855	0.22359	0.80888	0.17059
Computational time (second)	51	291	741	381	978

### 3.2. A spherical inclusion

The same cube as the previous example, which has a size of  $2 \text{ m} \times 2 \text{ m} \times 2 \text{ m}$  containing a spherical inclusion as schematically depicted in Fig. 11, is considered. The loading  $\sigma = 1 \text{ kPa}$  is applied to the six surfaces of the cube. A spherical inclusion radius of  $0.4 \text{ m}$  as shown in the figure, and a sphere center coordinate  $(x, y, z) = (0, 0, 0)$  are taken.

Due to the geometrical symmetry, only  $1/8$  of the cube is hence considered. To this end, Fig. 12a shows an initial mesh of  $6 \times 6 \times 6$  elements of  $1/8$  of the cube. Similarly, the tolerance error of this example of 5% is taken. The refined meshes discretized using the A-XFEM with either  $2 \times 2 \times 2$  or  $3 \times 3 \times 3$  sub-elements are shown in Figs. 12b and 12c, respectively. The figures representing the refined meshes indicate clearly that only interface region is refined,

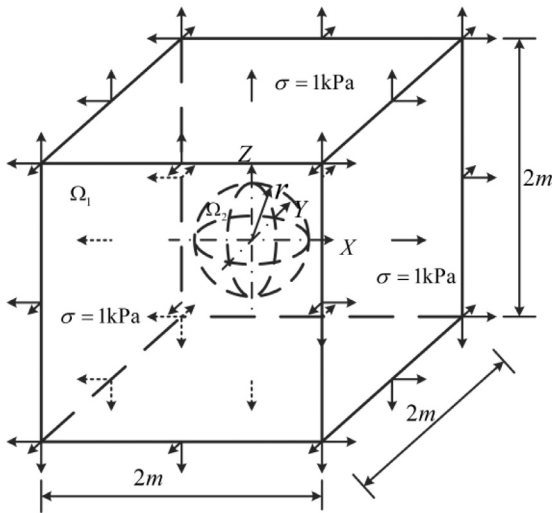


Fig. 11. Geometry of a cube containing a spherical inclusion and its configuration parameters showing the boundary and loading conditions.

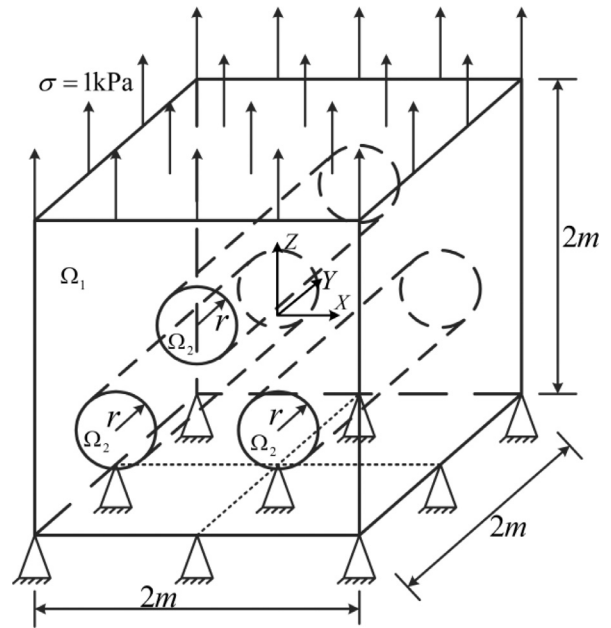


Fig. 13. Schematic configuration of a cube containing three cylindrical inclusions showing the boundary and loading conditions.

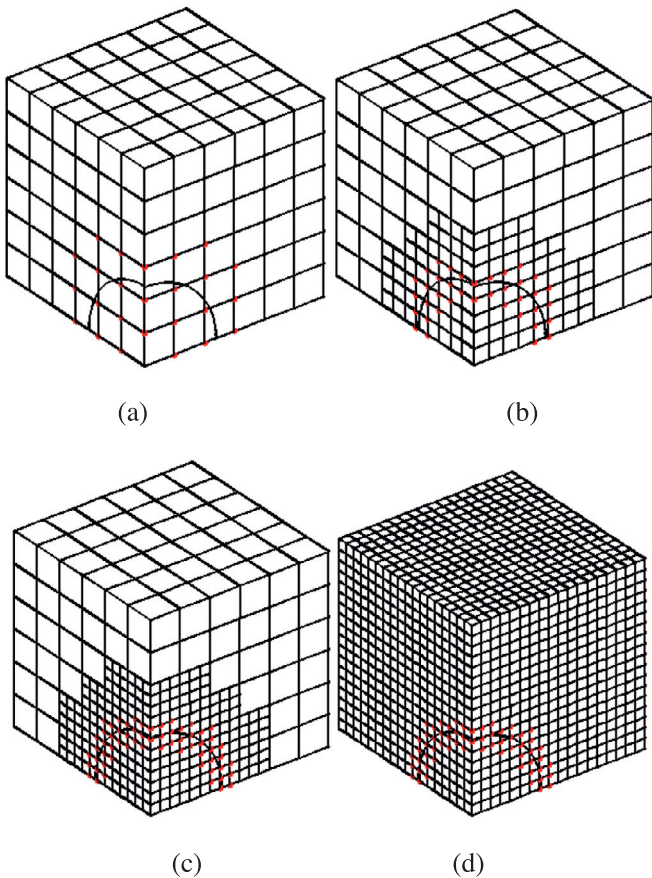


Fig. 12. 1/8 of a cube with a spherical inclusion: initial mesh (a); the refined A-XFEM mesh using  $2 \times 2 \times 2$  sub-elements (b) and  $3 \times 3 \times 3$  sub-elements (c); the conventional XFEM using  $18 \times 18 \times 18$  elements (d).

and this illustrates the main advantage of the proposed method in 3-D modeling.

Table 2 reports the strain  $L_2$  norm error estimated using the A-XFEM and conventional XFEM. The common XFEM results are performed using fine meshes of  $12 \times 12 \times 12$  and  $18 \times 18 \times 18$  elements. Only the mesh of  $18 \times 18 \times 18$  elements is shown in Fig. 12d. We note that the accuracy of the A-XFEM results are acceptable and in good agreement with that of the common XFEM, but

fewer DOFs for the A-XFEM (e.g., 675 and 1433) have been used, while the common XFEM takes a large number of DOFs (e.g., 2197 and 6859).

### 3.3. Three cylindrical inclusions

For multiple inclusions, we consider a  $2m \times 2m \times 2m$  cube containing three cylindrical inclusions as schematically depicted in Fig. 13. Each radius of the cylindrical inclusions is set to be  $0.2m$  and their  $(x, z)$  coordinates of the center of the cylinders are  $(1/2 m, -1/3 m)$ ,  $(-1/2 m, -1/3 m)$ ,  $(0 m, 1/3 m)$ , respectively. These cylindrical inclusions are fabricated through all the  $y$ -direction of the cube. The body is also subjected to a uniform traction of  $\sigma = 1kPa$  and the bottom surface is also constrained in all the directions.

Different from the above two examples, a tolerance error of 10% is taken for this multiple inclusions example. An initial mesh of  $10 \times 10 \times 10$  elements of this multiple inclusions cube is shown in Fig. 14a. The refined meshes using  $2 \times 2 \times 2$  and  $3 \times 3 \times 3$  sub-elements are also depicted in Figs. 14b and 14c. Two additional results used for comparison purpose obtained by the non-adaptive XFEM using fine meshes of  $20 \times 20 \times 20$  and  $30 \times 30 \times 30$  elements are provided, see Figs. 14d and 14e. As expected, it is found very similar to the single inclusion example, the refined meshes gained for multiple inclusions exhibit a very good performance of the proposed method as the refinement is only fulfilled at the interface between the inclusions and the matrix, which does not exist in the non-adaptive approach.

The strain  $L_2$  norm error are also estimated for the A-XFEM and the common XFEM. The obtained results of the strain  $L_2$  norm error are thus reported in Table 3. Not surprisingly, the same situation of the accuracy and the number of DOFs used for the A-XFEM is found. Compared to the common XFEM, the A-XFEM is the winner as it offers acceptable results with a significant less number of the DOFs.

### 3.4. Three spherical inclusions

We next perform multiple spherical inclusions by considering a  $2m \times 2m \times 2m$  cube containing three spherical inclusions as de-

**Table 2**

The strain  $L_2$  norm error obtained by the A-XFEM for different refinement methods. The conventional XFEM results are also added for the comparison purpose.

	Initial mesh	A-XFEM ( $2 \times 2 \times 2$ refinement)	A-XFEM ( $3 \times 3 \times 3$ refinement)	XFEM ( $12 \times 12 \times 12$ elements)	XFEM ( $18 \times 18 \times 18$ elements)
DOFs	343	675	1433	2197	6859
Strain $L_2$ norm error ( $\times 10^{-6}$ )	0.62346	0.07090	0.03778	0.06747	0.02756

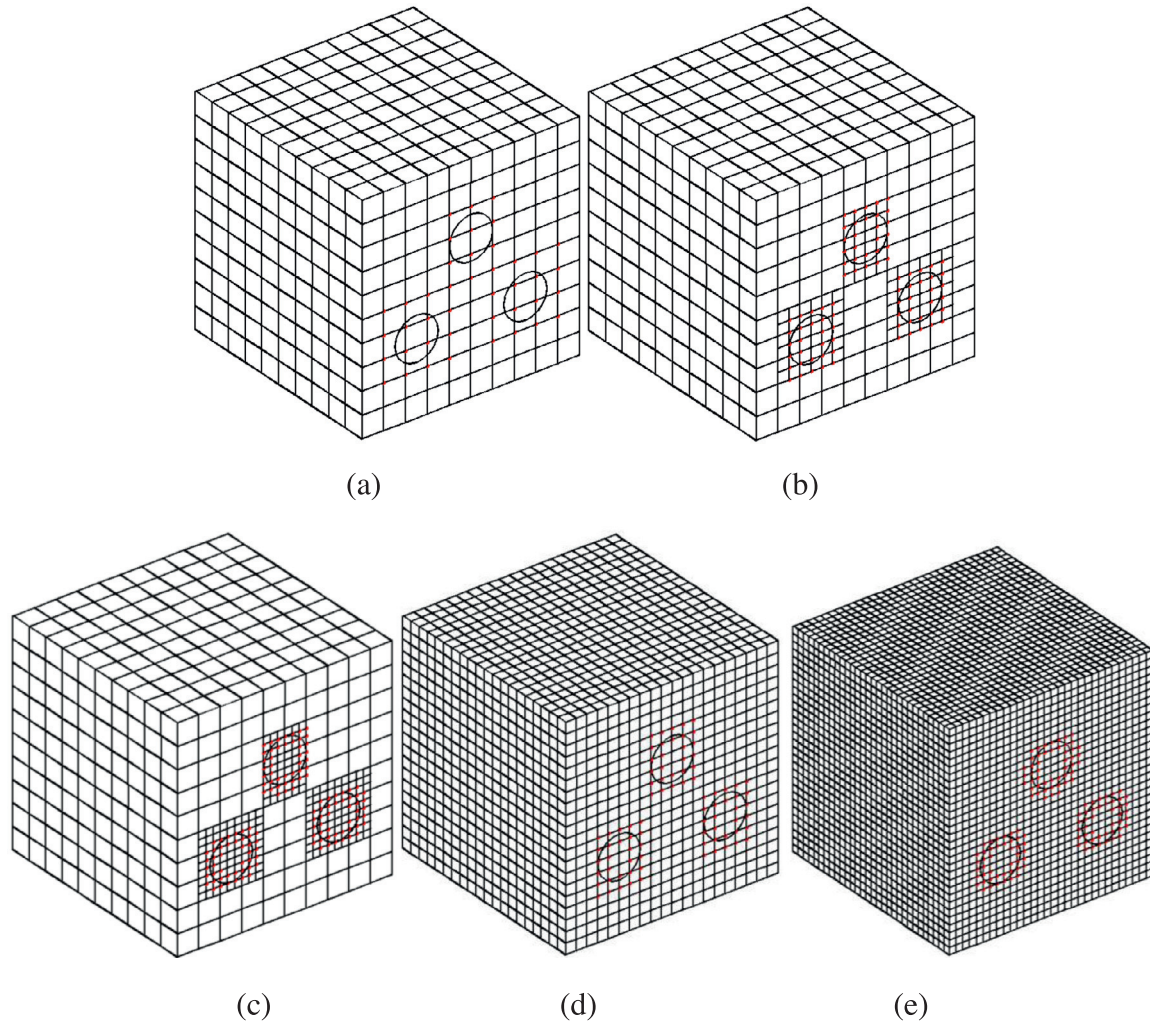


**Fig. 14.** A cube with three cylindrical inclusions: initial mesh (a); the refined A-XFEM mesh (using  $2 \times 2 \times 2$  sub-elements) (b); the refined A-XFEM mesh (using  $3 \times 3 \times 3$  sub-elements) (c); the conventional XFEM using  $20 \times 20 \times 20$  elements (d) and the conventional XFEM using  $30 \times 30 \times 30$  elements (e).

**Table 3**

The strain  $L_2$  norm error obtained by the A-XFEM for different refinement methods. The conventional XFEM results are also added for the comparison purpose.

	Initial mesh	A-XFEM ( $2 \times 2 \times 2$ refinement)	A-XFEM ( $3 \times 3 \times 3$ refinement)	XFEM ( $20 \times 20 \times 20$ elements)	XFEM ( $30 \times 30 \times 30$ elements)
DOFs	1331	3620	9177	9261	29,791
Strain $L_2$ norm error ( $\times 10^{-6}$ )	2.2297	0.5917	0.3780	0.4764	0.1692

picted in Fig. 15. The coordinate system is as follows: the origin locates at the center of the cube, the horizontal right direction is the X coordinate, the vertical inward direction is the Y coordinate, and the vertical upward direction is the Z coordinate. Each radius of the spherical inclusions is set to be 0.2 m and their sphere center coordinates are  $(1/2 \text{ m}, 0, -1/3 \text{ m})$ ,  $(-1/2 \text{ m}, 0, -1/3 \text{ m})$ ,  $(0, 0, 1/3 \text{ m})$ ,

respectively. The body is also subjected to a uniform traction of  $\sigma = 1 \text{ kPa}$  and the bottom surface is also constrained in all the direction.

Due to the geometrical symmetry with respect to the  $x$ - $z$  plane, half of the cube is taken. We also take a tolerance error of 10% for this example. The A-XFEM is applied to solve this three sphere in-

**Table 4**

The strain  $L_2$  norm error obtained by the A-XFEM for different refinement methods. The conventional XFEM results are also added for the comparison purpose.

	Initial mesh	A-XFEM ( $2 \times 2 \times 2$ refinement)	A-XFEM ( $3 \times 3 \times 3$ refinement)	XFEM ( $20 \times 10 \times 20$ elements)	XFEM ( $30 \times 15 \times 30$ elements)
DOFs	736	1035	1714	4851	15,376
Strain $L_2$ norm error ( $\times 10^{-6}$ )	0.3961	0.1338	0.0996	0.0969	0.0356

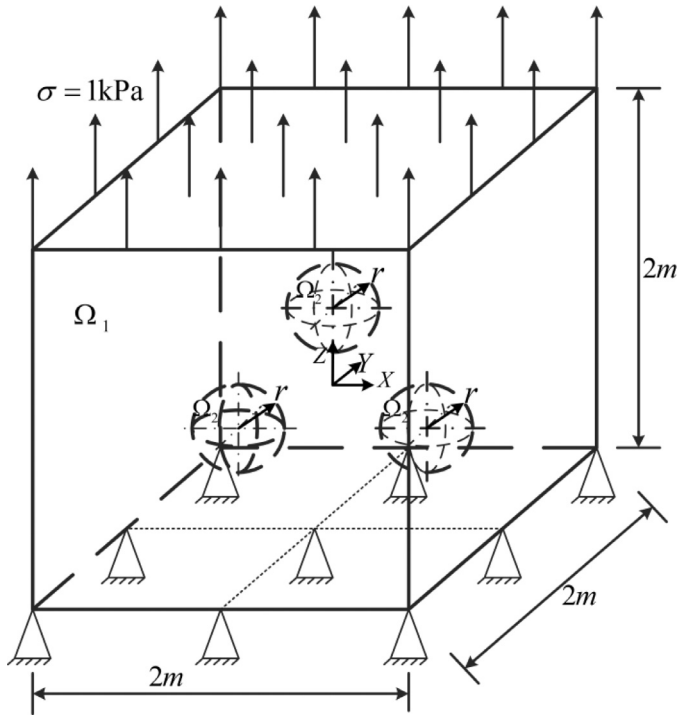


**Fig. 15.** Schematic configuration of a cube containing three spherical inclusions showing the boundary and loading conditions.

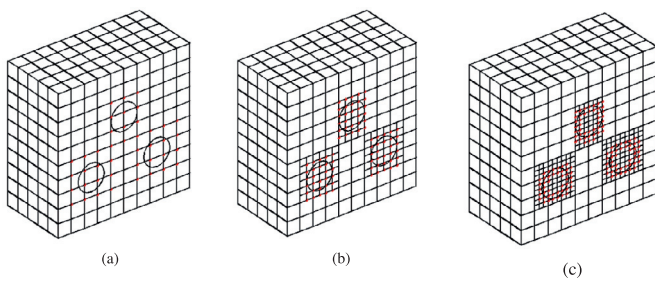


**Fig. 16.** Half of a cube with three spherical inclusions: initial mesh (a); the refined A-XFEM mesh using  $2 \times 2 \times 2$  sub-elements (b); the refined A-XFEM mesh using  $3 \times 3 \times 3$  sub-elements (c).

clusions problem, and an initial mesh of  $10 \times 5 \times 10$  elements of half of the cube is discretized as the first step of refinement, see Fig. 16a. Figs. 16b and 16c show the computed mesh refinements that are utilized using  $2 \times 2 \times 2$  and  $3 \times 3 \times 3$  sub-elements. A good performance of the proposed A-XFEM is found as region around the connection between two materials is refined only. Table 4 also reports the computed strain  $L_2$  norm error using the A-XFEM and conventional XFEM. The most important issue by means of the effectiveness (less DOFs) of the refinement approach is found.

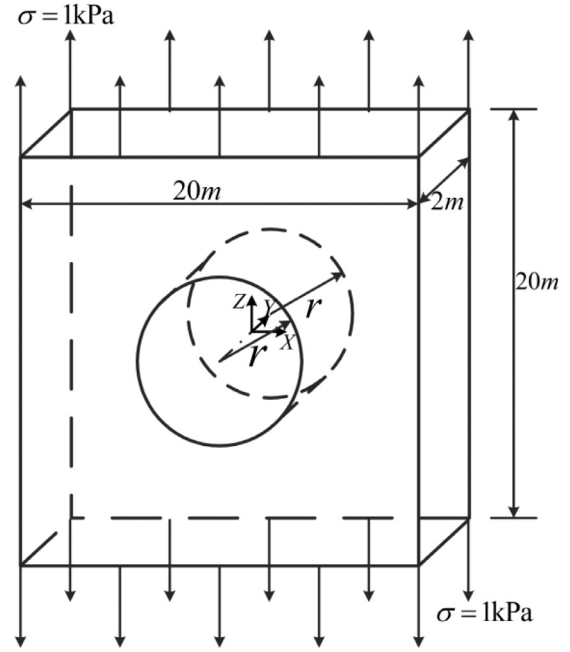


**Fig. 17.** Schematic configuration of a finite thickness plate with a cylindrical hole showing the boundary and loading conditions.

#### 4. Numerical examples of single and multiple voids (or holes)

Similar to the previous section, four examples are studied in this section, but dealing with single and multiple voids or holes instead. If not stated otherwise the following material constants are taken for all numerical examples: the Young's modulus  $E = 1000$  GPa and the Poisson ratio  $\nu = 0.3$ .

##### 4.1. A cylindrical hole

This example is mainly devoted to study 3-D void or hole using the present method. A finite thickness large plate containing a hole subjected to uniaxial tension  $\sigma = 1$  kPa acting on the top and the bottom of the plate as shown in Fig. 17. The width, thickness and height are  $20\text{ m} \times 2\text{ m} \times 20\text{ m}$ , the hole's center coordinate  $(x, z)$  is  $(0, 0)$ , and the cylindrical hole radius is 1 m. We only take 1/8 plate for the analysis because of geometrical symmetry. In this example, two different sets of subdivisions elements or children elements e. g.,  $2 \times 2 \times 2$  and  $3 \times 3 \times 3$ , are considered. We again specify the tolerance error of 5%. An initial mesh of  $10 \times 1 \times 10$  elements as sketched in Fig. 18a is taken, and the refined meshes derived from the A-XFEM for the two subdivisions of  $2 \times 2 \times 2$  and  $3 \times 3 \times 3$  children elements of first step are shown in Figs. 18b and 18c, and two fine meshes of  $20 \times 2 \times 20$  and  $30 \times 3 \times 30$  elements for the conventional XFEM are shown in Figs. 18d and 18e, respectively.

The exact solution to this problem is given in [44]. The displacement components in  $y=0$  are:

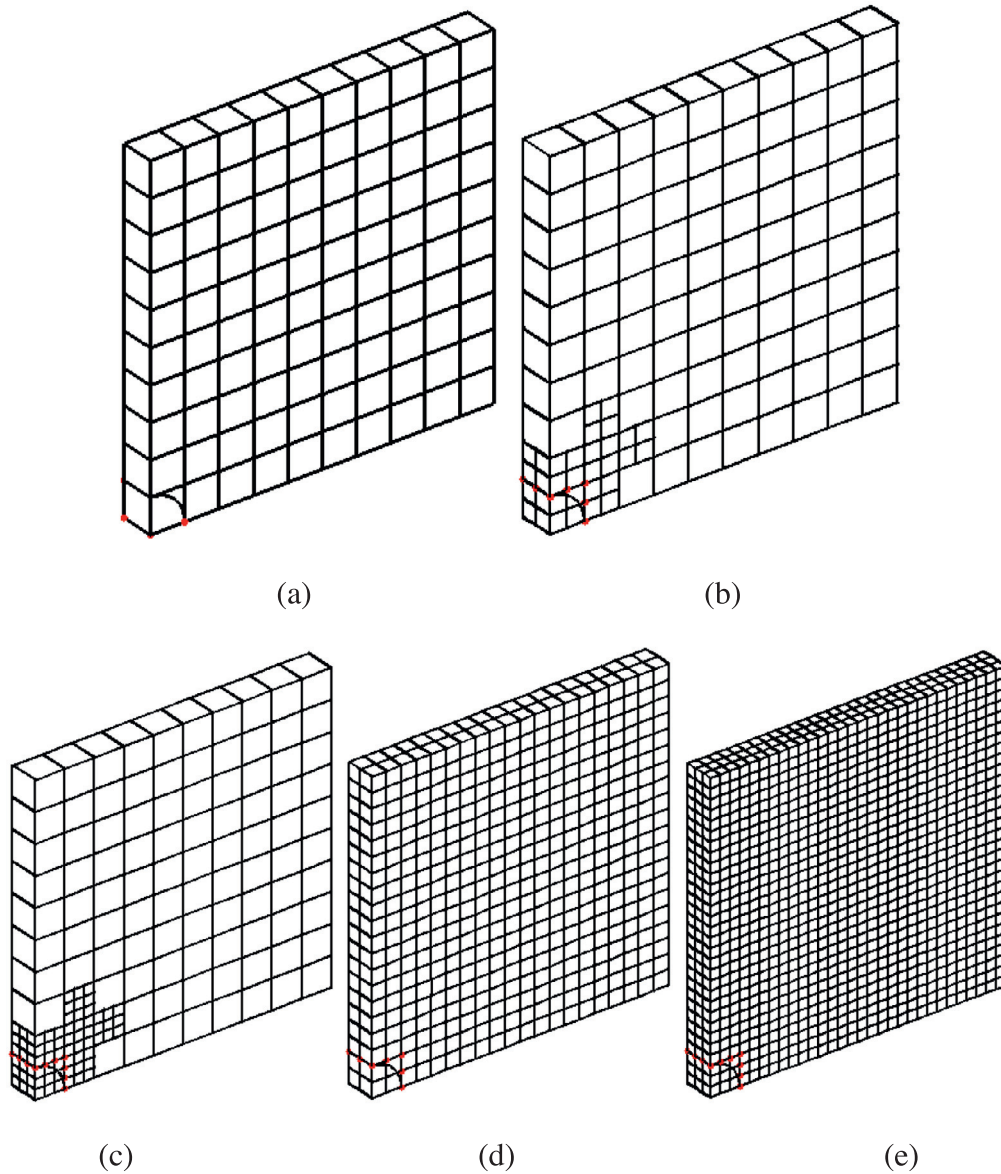


**Fig. 18.** 1/8 of a plate with a cylindrical hole: initial mesh (a); the refined A-XFEM mesh (using  $2 \times 2 \times 2$  sub-elements) (b); the refined A-XFEM mesh (using  $3 \times 3 \times 3$  sub-elements) (c); the conventional XFEM using  $20 \times 20$  elements (d) and the conventional XFEM using  $30 \times 30$  elements (e).

$$\begin{aligned}
 u_z(a, \theta) &= \frac{r}{8\mu} \left[ \frac{a}{r} (\kappa + 1) \cos \theta \right. \\
 &\quad \left. + 2 \frac{r}{a} ((1 + \kappa) \cos \theta + \cos 3\theta) - 2 \frac{r^3}{a^3} \cos 3\theta \right] \\
 u_x(a, \theta) &= \frac{r}{8\mu} \left[ \frac{a}{r} (\kappa - 3) \sin \theta \right. \\
 &\quad \left. + 2 \frac{r}{a} ((1 - \kappa) \sin \theta + \sin 3\theta) - 2 \frac{r^3}{a^3} \sin 3\theta \right] \quad (31)
 \end{aligned}$$

where  $(a, \theta)$  means the distance and the angle to the cylindrical center  $(x, z) = (0, 0)$  and  $\mu$  is the shear modulus and  $\kappa$  (Koloso constant) is defined as

$$\kappa = \begin{cases} 3 - 4\nu & \text{(plane strain)} \\ \frac{3 - \nu}{1 + \nu} & \text{(plane stress)} \end{cases} \quad (32)$$

As shown in Fig. 19, the accuracy of  $u_z$  computed by the A-XFEM increases with the aid of the refinement as compared with the analytical solutions. The accuracy is found the same as the

common XFEM using a fine mesh. So the computational efficiency of the A-XFEM is better than that of the conventional XFEM. Table 5 presents the strain  $L_2$  norm error result for refinements and the common XFEM. The advantage and effectiveness of A-XFEM over the conventional XFEM by means of the accuracy and the number of DOFs is found.

#### 4.2. A spherical hole

Next, we study a  $2\text{ m} \times 2\text{ m} \times 2\text{ m}$  cube containing a spherical hole as depicted in Fig. 20. The loading  $\sigma = 1\text{ kPa}$  is applied to the six surfaces of the cube. The spherical hole radius of  $0.4\text{ m}$  as shown in the figure is taken and the sphere center coordinate  $(x, y, z) = (0, 0, 0)$ . Only 1/8 of the cube is taken for the analysis. The refinement is applied to solve the problem of 1/8 of the cube using an initial mesh of  $6 \times 6 \times 6$  elements, see Fig. 21a. A tolerance error used for this example is 10%. The refined meshes results are shown in Fig. 21b and c, and their computed strain  $L_2$  norm errors are tabulated in Table 6. The same behaviors of the results and

**Table 5**

The strain  $L_2$  norm error obtained by the A-XFEM for different refinement methods. The conventional XFEM results are also added for the comparison purpose.

	Initial mesh	A-XFEM ( $2 \times 2 \times 2$ refinement)	A-XFEM ( $3 \times 3 \times 3$ refinement)	XFEM ( $20 \times 2 \times 20$ elements)	XFEM ( $30 \times 3 \times 30$ elements)
DOFs	242	327	508	1323	3844
Strain $L_2$ norm error ( $\times 10^{-6}$ )	2.1339	1.2707	0.8147	1.2700	0.7769

**Table 6**

The strain  $L_2$  norm error obtained by the A-XFEM for different refinement methods. The conventional XFEM results are also added for the comparison purpose.

	Initial mesh	A-XFEM ( $2 \times 2 \times 2$ refinement)	A-XFEM ( $3 \times 3 \times 3$ refinement)	XFEM ( $12 \times 12 \times 12$ elements)	XFEM ( $18 \times 18 \times 18$ elements)
DOFs	343	731	1641	2197	6859
Strain $L_2$ norm error ( $\times 10^{-6}$ )	0.46977	0.09340	0.07691	0.09322	0.05237

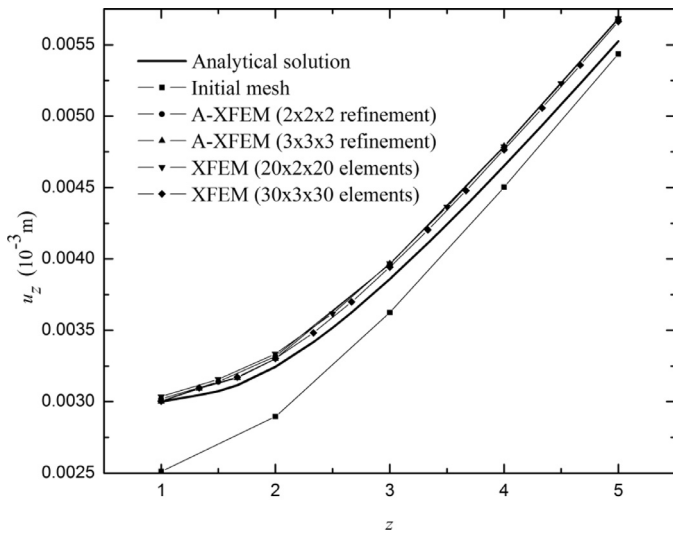


**Fig. 19.** Comparison of the  $u_z$  in  $x = 0, y = 0, z = 1 \text{ m} \sim 5 \text{ m}$  for a cube with a cylindrical hole among the A-XFEM, the conventional XFEM and the exact solution.

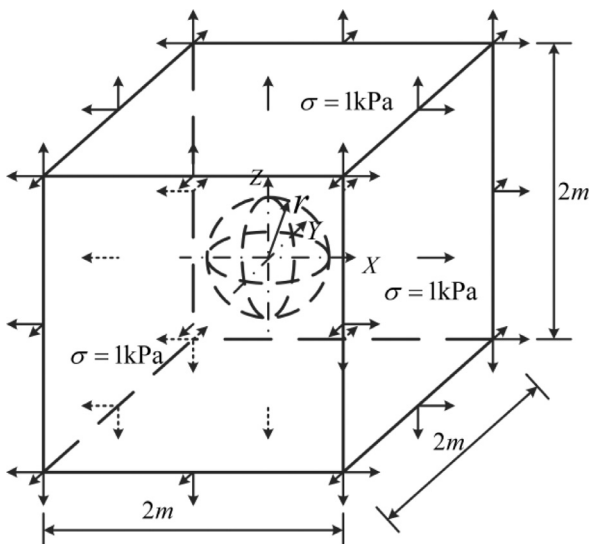


**Fig. 20.** Schematic configuration of a cube with a spherical hole showing the boundary and loading conditions.

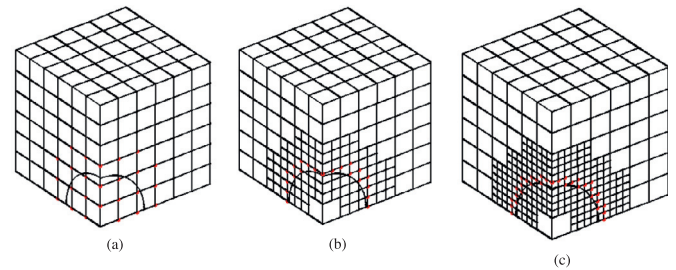


**Fig. 21.** 1/8 of a cube with a spherical hole: initial mesh (a); the refined A-XFEM mesh (using  $2 \times 2 \times 2$  sub-elements) (b); the refined A-XFEM mesh (using  $3 \times 3 \times 3$  sub-elements) (c).

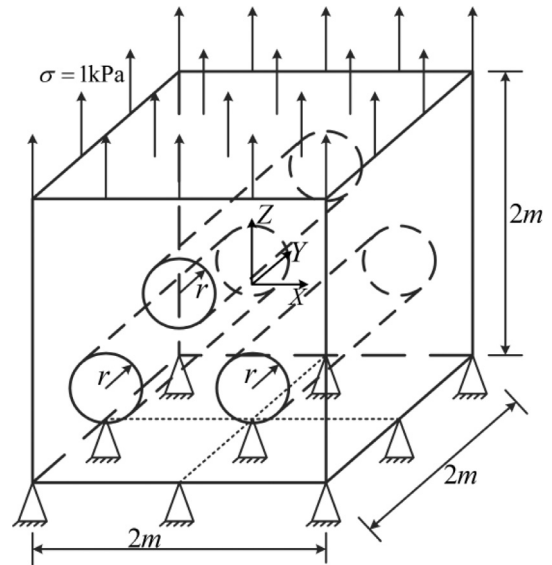


**Fig. 22.** Schematic configuration of a cube with three cylindrical holes showing the boundary and loading conditions.

the accuracy and good performance are again found in this single spherical hole example.

**4.3. Three cylindrical holes**

Next, we wanted to test the performance of the refinement procedure applied to a  $2 \text{ m} \times 2 \text{ m} \times 2 \text{ m}$  cube containing three cylindrical holes as shown in Fig. 22. Each radius of the cylindrical holes is  $0.2 \text{ m}$  and their central axis ( $x, z$ ) coordinates

**Table 7**

The strain  $L_2$  norm error obtained by the A-XFEM for different refinement methods. The conventional XFEM results are also added for the comparison purpose.

	Initial mesh	A-XFEM ( $2 \times 2 \times 2$ refinement)	A-XFEM ( $3 \times 3 \times 3$ refinement)	XFEM ( $20 \times 20 \times 20$ elements)	XFEM ( $30 \times 30 \times 30$ elements)
DOFs	1331	4819	13,331	9261	29,791
Strain $L_2$ norm error ( $\times 10^{-6}$ )	1.8830	0.5212	0.2979	0.4928	0.2486

**Table 8**

The strain  $L_2$  norm error obtained by the A-XFEM for different refinement methods. The conventional XFEM results are also added for the comparison purpose.

	Initial mesh	A-XFEM ( $2 \times 2 \times 2$ refinement)	A-XFEM ( $3 \times 3 \times 3$ refinement)	XFEM ( $20 \times 10 \times 20$ elements)	XFEM ( $30 \times 15 \times 30$ elements)
DOFs	726	1359	2812	4851	15,376
Strain $L_2$ norm error ( $\times 10^{-6}$ )	0.9295	0.3031	0.1611	0.2828	0.1220

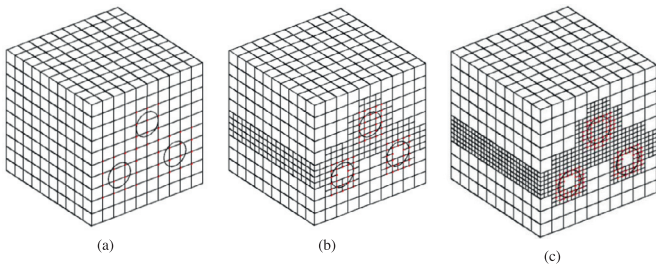


**Fig. 23.** A cube with three cylindrical holes: initial mesh (a); the refined A-XFEM mesh using  $2 \times 2 \times 2$  sub-elements (b); the refined A-XFEM mesh using  $3 \times 3 \times 3$  sub-elements (c).

are  $(1/2 \text{ m}, -1/3 \text{ m})$ ,  $(-1/2 \text{ m}, -1/3 \text{ m})$ ,  $(0 \text{ m}, 1/3 \text{ m})$ , respectively. These cylindrical holes are fabricated through all the  $y$  direction of the cube. The body is also subjected to a uniform traction of  $\sigma = 1 \text{ kPa}$  and the bottom surface is also constrained in all the direction. Fig. 23 reveals a good performance of the developed A-XFEM since the refinement is only fulfilled at the interface among the holes and the matrix. The estimated strain  $L_2$  norms obtained are tabulated in Table 7. We have examined the accuracy of the method and the same results as observed in the above examples are found.

#### 4.4. Three spherical holes

The last example deals with a  $2 \text{ m} \times 2 \text{ m} \times 2 \text{ m}$  cube containing three spherical holes as depicted in Fig. 24. The coordinate system is detailed as follows: the origin locates at the center of the cube; the horizontal right direction:  $X$  coordinate; the vertical inward direction:  $Y$  coordinate; and the vertical upward direction:  $Z$  coordinate. Each radius of the hole is  $0.2 \text{ m}$  and their sphere center coordinates are  $(1/2 \text{ m}, 0, -1/3 \text{ m})$ ,  $(-1/2 \text{ m}, 0, -1/3 \text{ m})$ ,  $(0, 0, 1/3 \text{ m})$ , respectively. The top surface is also subjected to a uniform traction of  $\sigma = 1 \text{ kPa}$  and the bottom surface is also constrained in all the direction. Due to the geometrical symmetry with respect to the  $X$ - $Z$  plane, we also pick half of the cube for this example. A tolerance error of 10% is taken for this analysis. Fig. 25a shows an initial mesh of  $10 \times 5 \times 10$  elements. Refined meshes are also depicted in Figs. 25b and 25c exhibiting, once again, a good performance of the adaptive algorithm. We additionally report the strain  $L_2$  norm error estimated using A-XFEM and the conventional XFEM as in Table 8, by which the effectiveness of the method is confirmed.

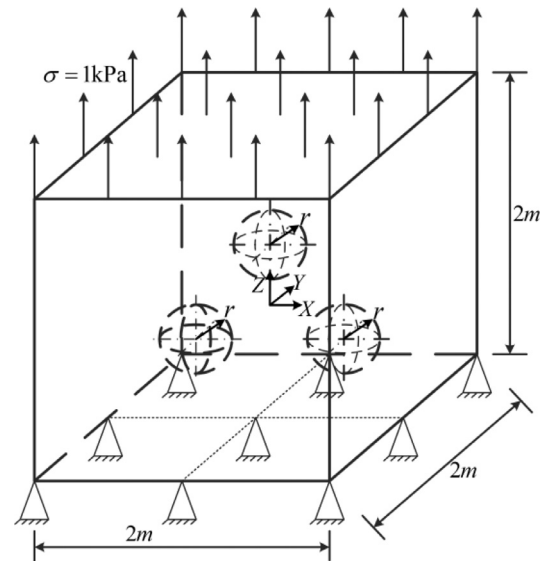


**Fig. 24.** Schematic configuration of a cube with three spherical holes showing the boundary and loading conditions.

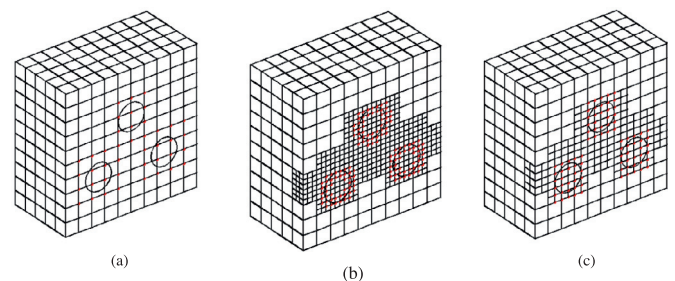


**Fig. 25.** Half of a cube with three spherical holes: initial mesh (a); the refined A-XFEM mesh using  $2 \times 2 \times 2$  sub-elements (b); the refined A-XFEM mesh using  $3 \times 3 \times 3$  sub-elements (c).

## 5. Conclusions and outlook

We have developed an effective 3-D adaptive XFEM for accurately modeling holes and inclusions. This 3-D approach is driven by a *posteriori* recovery-based error estimation to detect all elements that will be refined in the next refinement step. The variable-node elements are taken in order to treat the mismatching problems of different scale-meshes. The local mesh refinement

strategy proposed here reflects the robustness of effective numerical methods as the fine-scale mesh is only tackled to where it is required. We have examined a series of representative numerical examples including single and multiple inclusions and holes in 3-D, and the obtained numerical results, which are compared with analytical and common XFEM solutions, reveal good performance, effectiveness and accuracy of the developed method.

We have found through the numerical investigation that by using the adaptive algorithm, which makes the proposed A-XFEM possible to improve the accuracy of the interface region. Moreover, the A-XFEM carries with less DOFs than those through the XFEM. Consequently, the approach is found highly suitable for practices, and its further applications to more complicated problems such as the aggregated composites are possible. Some of the main challenges of the proposed method in modeling these complicated problems can be briefly given as follows: (1) Each interface is described with one level set function, so the level set function for complex geometry would be one major challenge; (2) If a large proportion of inclusions are included in the model of interest, fine mesh should be used for the whole domain, requiring a large amount of computational effort, as a consequence the advantage of the A-XFEM for this particular case may not be obvious; (3) Modeling multiple matrix cracking and delamination may also be another challenge.

Like the conventional XFEM, the proposed A-XFEM in general can also be used to model the periodic structures/boundary condition. The challenges in modeling the periodic structures/boundary condition would be the same as those in modeling the aggregated composites, which are already addressed above.

Nonetheless, the present work only concerns with the inclusions with perfect interfaces. For imperfect interfaces problems, the enrichment function  $\Psi(\mathbf{x})$  may have to be chosen as the Heaviside step function and the crack-tip branch enrichment functions. The adaptive numerical framework for other interface jump conditions is the same as that proposed in this paper, it is noted that the smoothed field for the *posterior* error estimation must be reconstructed.

## Acknowledgments

Tiantang Yu was supported by the National Sci-Tech Support Plan of China (Grant No. 2015BAB07B10) and the National Natural Science Foundation of China (Grant No. 51179063); Tinh Quoc Bui was supported by the Grant-in-Aid for Scientific Research – JSPS; Nguyen Thi Hien Luong was supported by the Vietnam Foundation for Science and Technology (NAFOSTED). Nguyen Dinh Duc was supported by Vietnam Foundation for Science and Technology (NAFOSTED) under grant number 107.02-2015.03. The financial supports are gratefully acknowledged. Tinh Quoc Bui is also grateful to Professor Sohichi Hirose, Tokyo Institute of Technology, Japan for his support throughout the course of this work. The authors also would like to thank the anonymous reviewers for their valuable comments and helpful suggestions to improve the quality of the present work.

## References

- [1] Guidault PA, Allix O, Champany L, Cornuault C. A multiscale extended finite element method for crack propagation. *Comput Methods Appl Mech Eng* 2008;197:381–99.
- [2] Loehnert S, Belytschko T. A multiscale projection method for macro/microcrack simulations. *Int J Numer Meth Eng* 2007;71:1466–82.
- [3] de Boer A, van Zuijlen AH, Bijl H. Review of coupling methods for nonmatching meshes. *Comput Methods Appl Mech Eng* 2007;196:1515–25.
- [4] Puso MA. A three-dimensional mortar method for solid mechanics. *Int J Numer Meth Eng* 2002;59:315–36.
- [5] Dhia HB, Rateau G. The Arlequin method as a flexible engineering design tool. *Int J Numer Meth Eng* 2005;62:1442–62.
- [6] Belytschko T, Black T. Elastic crack growth in finite elements with minimal remeshing. *Int J Numer Meth Eng* 1999;45:601–20.
- [7] Bui QT, Zhang C. Extended finite element simulation of stationary dynamic cracks in piezoelectric solids under impact loading. *Comp Mater Sci* 2012;62:243–57.
- [8] Yu TT. The extended finite element method (XFEM) for discontinuous rock masses. *Eng Comput* 2011;28(3):340–69.
- [9] Yu TT, Liu P. Improved implementation of the extended finite element method for stress analysis around cracks. *Arch Civ Mech Eng* XI(3) 2011:787–805.
- [10] Yu TT, Shi LY. Determination of sharp V-notch stress intensity factors using the extended finite element method. *J Strain Anal Eng* 2012;47(2):95–103.
- [11] Liu P, Yu TT, Bui TQ, Zhang C. Transient dynamic crack analysis in non-homogeneous functionally graded piezoelectric materials by the X-FEM. *Comp Mater Sci* 2013;69:542–58.
- [12] Liu P, Yu TT, Bui TQ, Zhang C, Xu YP. Transient thermal shock fracture analysis of functionally graded piezoelectric materials by the extended finite element method. *Int J Solids Struct* 2014;51(11–12):2167–82.
- [13] Liu P, Bui TQ, Zhu D, Yu TT, Wang JW, Yin SH, et al. Buckling failure analysis of cracked functionally graded plates by a stabilized discrete shear gap extended 3-node triangular plate element. *Compos Part B* 2015;77:179–93.
- [14] Yu TT, Bui TQ, Liu P, Zhang C, Hirose S. Interfacial dynamic impermeable cracks analysis in dissimilar piezoelectric materials under coupled electromechanical loading with the extended finite element method. *Int J Solids Struct* 2015;67–68:205–16.
- [15] Kang Z, Bui QT, Nguyen DD, Saitoh T, Hirose S. An extended consecutive-interpolation quadrilateral element (XCQ4) applied to linear elastic fracture mechanics. *Acta Mech* 2015;226:3991–4015.
- [16] Bhattacharya S, Singh IV, Mishra BK, Bui QT. Fatigue crack growth simulations of interfacial cracks in bi-layered FGMs using XFEM. *Comput Mech* 2013;52:799–814.
- [17] Zhang XD, Bui QT. A fictitious crack XFEM with two new solution algorithms for cohesive crack growth modeling in concrete structures. *Eng Comput* 2015;32:473–97.
- [18] Bui QT, Zhang C. Analysis of generalized dynamic intensity factors of cracked magnetoelastoelectric solids by X-FEM. *Finite Elem Anal Des* 2013;69:19–36.
- [19] Sharma K, Bui QT, Zhang C, Bhargava RR. Analysis of a subinterface crack in piezoelectric bimetals with the extended finite element method. *Eng Fract Mech* 2013;104:114–39.
- [20] Yu TT, Bui QT, Liu P, Hirose S. A stabilized discrete shear gap extended finite element for the analysis of cracked Reissner-Mindlin plate vibration problems involving distorted meshes. *Int J Mech Mater Des* 2016;12(1):85–107.
- [21] Shi LY, Yu TT, Bui QT. Numerical modeling of hydraulic fracturing in rock mass by XFEM. *Soil Mech Found Eng* 2015;52:74–83.
- [22] Pathak H, Singh A, Singh IV, Yadav SK. A simple and efficient XFEM approach for 3-D cracks simulations. *Int J Fract* 2013;181:189–208.
- [23] Pathak H, Singh A, Singh IV, Yadav SK. Fatigue crack growth simulations of 3-D linear elastic cracks under thermal load by XFEM. *Front Struct Civil Eng* 2015;9:359–82.
- [24] Pathak H, Singh A, Singh IV. Fatigue crack growth simulations of 3-D problems using XFEM. *Int J Mech Sci* 2013;76:112–31.
- [25] Pathak H, Singh A, Singh IV. Numerical simulation of bi-material interfacial cracks using EFGM and XFEM. *Int J Mech Mater Des* 2012;8:9–36.
- [26] Pathak H, Singh A, Singh IV. Fatigue crack growth simulations of bi-material interfacial cracks under thermo-elastic loading by extended finite element method. *Eur J Comput Mech* 2013;22:79–104.
- [27] Singh IV, Mishra BK, Bhattacharya S, Patil RU. The numerical simulation of fatigue crack growth using extended finite element method. *Int J Fatigue* 2012;36:109–19.
- [28] Prange C, Loehnert S, Wriggers P. Error estimation for crack simulations using the XFEM. *Int J Numer Meth Eng* 2012;91:1459–74.
- [29] Loehnert S, Prange C, Wriggers P. Error controlled adaptive multiscale XFEM simulation of cracks. *Int J Fract* 2012;178:147–56.
- [30] Holl M, Loehnert S, Wriggers P. An adaptive multiscale method for crack propagation and crack coalescence. *Int J Numer Meth Eng* 2013;93:23–51.
- [31] Soghrati S, Duarte CA, Geubelle HP. An adaptive interface-enriched generalized FEM for the treatment of problems with curved interfaces. *Int J Numer Meth Eng* 2015;102:1352–70.
- [32] Rannou J, Gravouil A, Baitto-Dubourg MC. A local multigrid X-FEM strategy for 3-D crack propagation. *Int J Numer Meth Eng* 2009;77:581–600.
- [33] Fries TP, Byfut A, Alizada A, Cheng KW, Schroder A. Hanging nodes and XFEM. *Int J Numer Meth Eng* 2011;86:404–30.
- [34] Dulfot M, Bordas S. A posteriori error estimation for extended finite elements by an extended global recovery. *Int J Numer Meth Eng* 2008;76:1123–38.
- [35] Zienkiewicz OC, Zhu JZ. A simple error estimator and adaptive procedure for practical engineering analysis. *Int J Numer Meth Eng* 1987;24:337–57.
- [36] Sohn D, Lim JH, Im S. An efficient scheme for coupling dissimilar hexahedral meshes with the aid of variable-node transition elements. *Adv Eng Softw* 2013;65:200–15.
- [37] Lim JH, Sohn D, Im S. Variable-node element families for mesh connection and adaptive mesh computation. *Struct Eng Mech* 2012;43:349–70.
- [38] Moës N, Cloirec M, Cartraud P, Remacle JF. A computational approach to handle complex microstructure geometries. *Comput Methods Appl Mech Eng* 2003;192(28–30):3163–77.
- [39] Sukumar N, Chopp DL, Moës N, Belytschko T. Modeling holes and inclusions by level sets in the extended finite-element method. *Comput Methods Appl Mech Eng* 2001;190:6183–200.

- [40] Ventura G, Gracie R, Belytschko T. Fast integration and weight function blending in the extended finite element method. *Int J Numer Meth Eng* 2009;77:1–29.
- [41] Seabra RRM, Cesar de Sa MAJ, Sustaric P, Rodic T. Some numerical issues on the use of XFEM for ductile fracture. *Comput Mech* 2012;50:611–29.
- [42] Natarajan S, Roy Mahapatra D, Bardas PAS. Integrating strong and weak discontinuities without integration subcells and example applications in an XFEM/GFEM framework. *Int J Numer Meth Eng* 2010;83:269–94.
- [43] Khosravifard A, Hematiyan MR. A new method for meshless integration in 2D and 3D Galerkin meshfree methods. *Eng Anal Bound Elem* 2010;34:30–40.
- [44] Szabó B, Babuška I. *Introduction to finite element Analysis: Formulation, verification and validation*. United Kingdom: John Wiley & Sons Ltd; 2011.